Nonlinear dynamics of an autonomous robot with deformable origami wheels

Larissa M. Fonseca, Marcelo A. Savi *

Center for Nonlinear Mechanics, COPPE – Department of Mechanical Engineering, Universidade Federal do Rio de Janeiro, 21.941.972 – Rio de Janeiro – RJ, P.O. Box 68.503, Brazil

ARTICLE INFO

ABSTRACT

Autonomous robots have several applications on industry, military and safety fields. The replacement of the conventional wheels by deformable ones improves the maneuverability, allowing it to trespass obstacles that goes from small fissures to step elevations. Besides, path control can be made by directly actuation on the wheel using a small number of actuators, reducing the structure weigh. This paper deals with a dynamical analysis of an autonomous robot with origami wheels actuated by shape memory alloys (SMAs), forming a self-foldable structure. The nonlinear characteristics of the SMAs together with the slender and bi-stable origami aspects provide a complex nonlinear behavior that can be exploited for energetic and maneuverability purposes. Mathematical modeling considers a reduced order model, based on symmetry hypotheses, to describe the origami mechanics. In addition, a polynomial constitutive model is employed to describe the thermomechanical behavior of the SMA actuators. The robot dynamics is described by considering a rigid body system connected to the two origami wheels. Under these assumptions, the robot dynamical model is represented by a 4-degree of freedom system. The yaw rotation, that promotes the route change, is promoted by the origami radius variation. Numerical simulations related to operational conditions are carried out considering different operational conditions represented by distinct thermal and mechanical loads. Results show situations where different external stimulus can promote interesting nonlinear dynamical responses including chaos, transient chaos and synchronization.

1. Introduction

Origami paper-folding art has been exploited on several areas of human knowledge due to its compactness, adaptive capacity and morphing ability. In brief, it produces a three-dimensional structure from the folding of a two-dimensional source. Shapes emerging from cylindrical or spherical configurations, as the combination of morphing capable elements, can be applied on architecture [1], robotic [2], spatial systems [3] and biomedical devices [4].

The use of origami in mechanical systems has an increasing interest. Textured tubes for subsea operations have the potential to reduce the propagation buckling without increasing the wall thickness of the pipeline. In this case, origami assumes a rigid configuration, and the purpose is the stress accommodation [5–7]. A different application of a texturized tube is the zipper-coupled tube configuration that exploits the change on stiffness [8]. This combination can be made in a large variety of cellular assemblages, promoting mobility and versatility to the final system and enhancing its mechanical characteristics.

Biomedical devices are another type of origami application. The origami stent is a deployable cylinder that has the advantage with respect to the classical cardiovascular device since it avoids the restenosis effect [9]. The biomedical origami robots are biocompatible and biodegradable self-folding devices that can be encapsulated on ice for delivery through the esophagus, transporting drug layer that is passively released to a wounded area [10]. These robots can be remotely controlled to perform underwater maneuvers, specifically using magnetic fields. This robot allows the removal of swallowed battery without the need of a surgery.

The idea of other types of robots is also an interesting subject related to origamis. Autonomous robots with self-folding origami wheels are a good alternative that provides alteration of torque–force transmission by changing the radius of the wheel [2,11]. Deformable wheels are interesting to improve maneuverability, allowing one to trespass obstacles that goes from small fissures to step elevations. Besides, the path control can be made by directly actuation on the wheel using a small number of actuators, significantly reducing the weight of the structure. One of the advantages is the easy control using each wheel independently [12].

Since origami systems are thin structures, they are usually close to stability limits with important dynamical issues to be investigated. The combination of geometric and constitutive nonlinearities is responsible for a rich dynamic behavior and, therefore, external excitations and perturbations can be critical to the system response and may be a

---

* Corresponding author.

E-mail addresses: larissamaciel.lah@gmail.com (L.M. Fonseca), savi@mecanica.coppe.ufrj.br (M.A. Savi).

problem in several applications. In this regard, dynamical analysis of these structures becomes particularly important, being treated in few references in the literature. Rodrigues et al. [13] investigated nonlinear dynamics of an origami stent. On the other hand, Fonseca et al. [14] investigated nonlinear dynamics of an origami wheel. Both references consider origami built with waterbomb pattern, assuming symmetric hypothesis related to the design and application in order to build a reduced order model. Although this simplification reduces the number of degrees of freedom, geometric and constitutive nonlinearities make the origami dynamical response very rich, presenting periodic and chaotic motions.

This paper deals with the dynamical analysis of an autonomous origami wheel robot, which has deformable wheels that provide path control. A rigid body motion analysis of the robot is carried out. The model is based on the positioning of the robot chassis and each wheel gravity centers. Deformable wheels are modeled by a reduced order model built based on the origami symmetries. Under this assumption, each origami wheel is analyzed from a one degree of freedom model, as discussed in Fonseca et al. [14]. The robot equations of motion are numerically solved in order to investigate the system dynamics. Different operational conditions are carried out showing the high sensitivity of the origami robot behavior. Complex responses are of concern highlighting chaos and synchronization. In this regard, this origami wheel robot analysis provides a new perspective into origami structure applications, allowing the potential use of rich nonlinear dynamics responses in order to furnish new desirable behaviors.

2. Origami wheel robot

Robots with deformable wheels have the potential to improve maneuverability providing path control and the capacity to overcome obstacles. The idea is to promote wheel size change by a direct actuation using shape memory alloy actuators. A two-wheeled robot is modeled considering deformable origami-based wheels. The robot is composed by a chassis with mass center G rigidly attached to weightless axes that are connected to two independent deformable origami wheels with mass centers G_A and G_B (Fig. 1-a). The chassis is built such that the mass centers G_A, G_B and G are always aligned and along the axis connecting the wheels. Besides, each wheel is attached to the axis in such a way that its mass center does not slide through the axis, *i.e.*, the mass centers of G_A and G_B are symmetrically positioned with respect to G at constant distance d (Fig. 1-b).

Each origami wheel is constructed by employing a 3×8 magic-ball or waterbomb pattern, which has been used in various applications. Waterbomb pattern can be considered as a rigidly foldable or rigid origami that consists of panels that can move continuously between folded configurations by rotating around the crease lines without deformation. The use of an origami wheel has the main objective to create an expandable structure that can alter its configuration in response to some external stimulus. In this regard, shape memory alloy (SMA) springs are placed on the origami circumferential direction, which can be thermal actuated to promote shape changing. Note that the unitary cell opening characterizes the SMA length (Fig. 2). Besides these SMA actuators, the system needs a passive bias elastic spring, placed in the longitudinal direction, ensuring the shape change of all the structure between two limit configurations (Fig. 2).

The origami wheel employs pre-trained SMA actuators, where the pre-stress is able to produce a reorientation from twinned martensitic crystallographic phase to detwinned martensite. Under this condition, the SMA spring has a residual displacement that can be recovered by heating the SMA, promoting a martensite–austenite phase transformation. This actuation process changes the shape of the wheel, reducing its radius. A typical force–displacement–temperature curve for the shape memory effect (SME) is shown in Fig. 3-a where, starting at a low temperature ($T < T_M$ - a temperature where martensitic phase is stable), the system is subjected to a mechanical loading cycle, resulting in
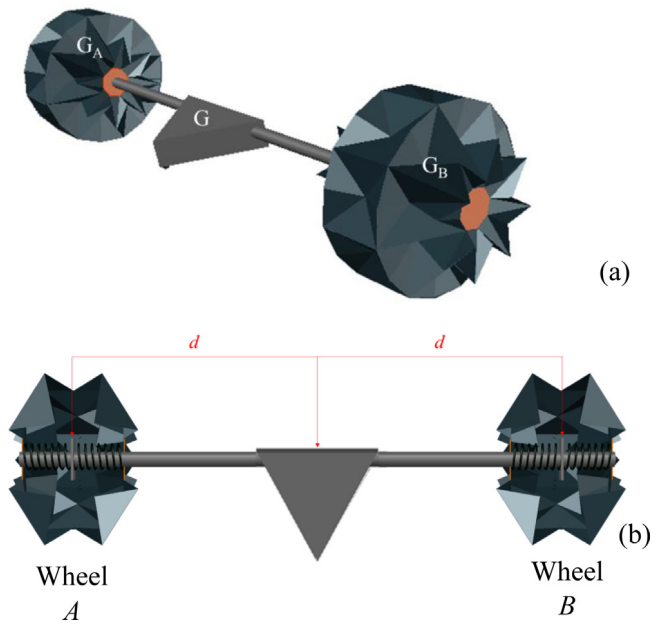

Fig. 1. Origami-wheel robot of two deformable wheels. (a) Isometric view with indications of the mass centers for the wheels, G_A and G_B, and mass center of the chassis, G; (b) Superior view, with cuttings on the wheels, for details of the attachment of the wheels to the axes.

a residual displacement. The recovering process is achieved by the heating of the SMA ($T > T_A$ - a temperature where austenitic phase is stable), inducing the transformation from martensite to austenite, promoting the shape recovery. Fig. 3-b shows the shape memory effect (SME) on a bias system, which means that the mechanical load applied deforms the shape memory spring at the lower temperature. The SME works against the force of the bias spring and, when the SMA spring is cooled down, the bias actuator promotes the reorientation process and therefore, the SMA spring changes between two configurations — low and high temperatures, associated with open and closed origami configurations.

The origami configuration change promotes the yaw motion that defines the moving direction of the origami robot. This can be evaluated by the radius variation that establishes a difference between the wheels, by heating/cooling the SMAs actuators. Based on that, in order to turn left (counterclockwise turn from wheel B to wheel A), a heating cycle is applied to the SMAs on the wheel A, reducing its radius and inducing a rotation to the left. At this point, a straight path is recovered by either heating up wheel B, which will lead both wheels to the closed configuration, or cooling down wheel A, which will lead both wheels to the opened configuration. Once both wheels have the same radius, the car keeps following a straight line.

3. Origami wheel model

Origami wheel is built by considering a waterbomb pattern that can be understood as a tessellation of a unitary cell defined by a 6-creased folding pattern (Fig. 4). This pattern belongs to a group of origami classified as rigidly foldable, once that all the folding process occurs on the creases only and the panels remain flat, without deformation. Fang et al. [15] developed a study of the origami wheel for different designs (number of columns and number of cells per column), verifying that even with the bending motion, the structure has a rigidly foldable region. They also showed operational ranges that are contained into the rigidly foldable region.

Besides rigid-foldability hypothesis, symmetry conditions can be assumed considering either geometric or external force conditions.
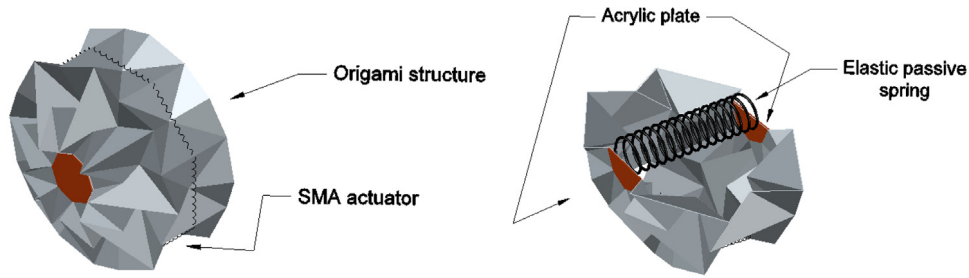
Fig. 2. Origami-wheel concept. The structure is actuated by 8 identical SMAs placed around its larger radius and the restitution is provided by an elastic spring attached to acrylic plates placed on the end points of the wheel.
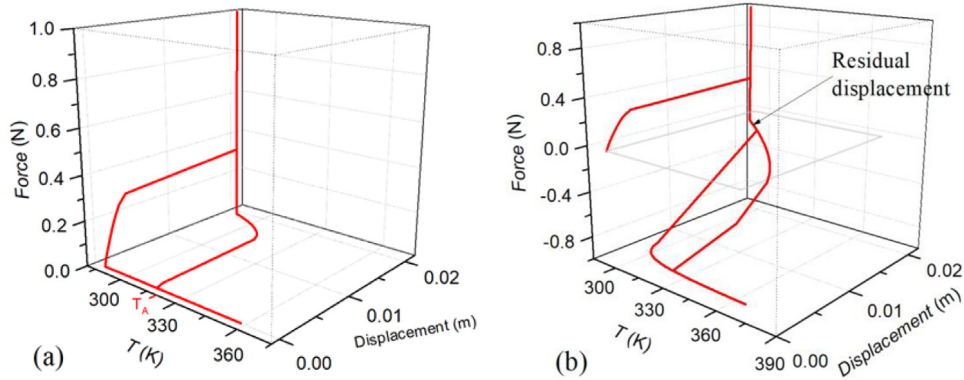

Fig. 3. Typical force–displacement–temperature curves for SMA springs: (a) shape memory effect (SME); (b) SME on a bias system.
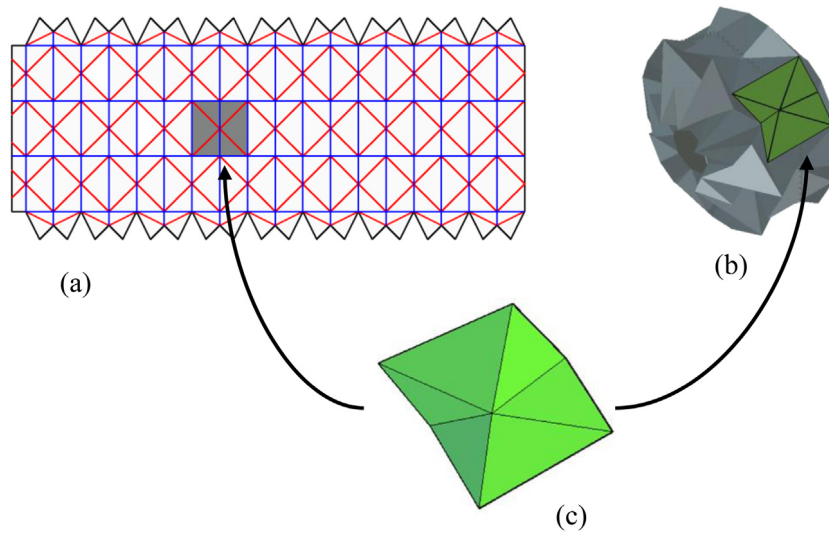

Fig. 4. Representation of a waterbomb tessellation in an opened configuration, showing the color-defined folds (mountain in blue and valley in red) (a), waterbomb tessellation in a closed configuration (b), and an unitary cell (c). The arrows represent the position of the highlighted unitary cell on each tessellation.. (For interpretation of the references to color in this figure legend, the reader is referred to the web version of this article.)

Based on that, rotational symmetry is observed, being related to axial movement during expansion, meaning that both ends are pulled equally, avoiding snaps on origami sides. Under these assumptions, a single cell is representative of the general origami wheel behavior. Fonseca et al. [14] established a description of the origami wheel considering symmetrical actuation, where the original complex system with multiple degrees of freedom can be reduced to a one-degree of freedom system. Fig. 5 defines a geometrical view of the structure, leading to geometric relations presented in Eqs. (1)–(5).

$$L_2 = b \sin \alpha + 2b \cos \beta - \frac{b}{2} \sin \beta \tag{1}$$

$$R_2 = r + 2b \sin \beta + \frac{b}{2} \cos \beta = R_1 + b \cos \alpha \tag{2}$$

$$L_1 = 2a \sin \theta \tag{3}$$

$$R_1 = a \left(\frac{\sin \theta}{\tan \frac{\pi}{8}} - \cos \theta \right) \tag{4}$$

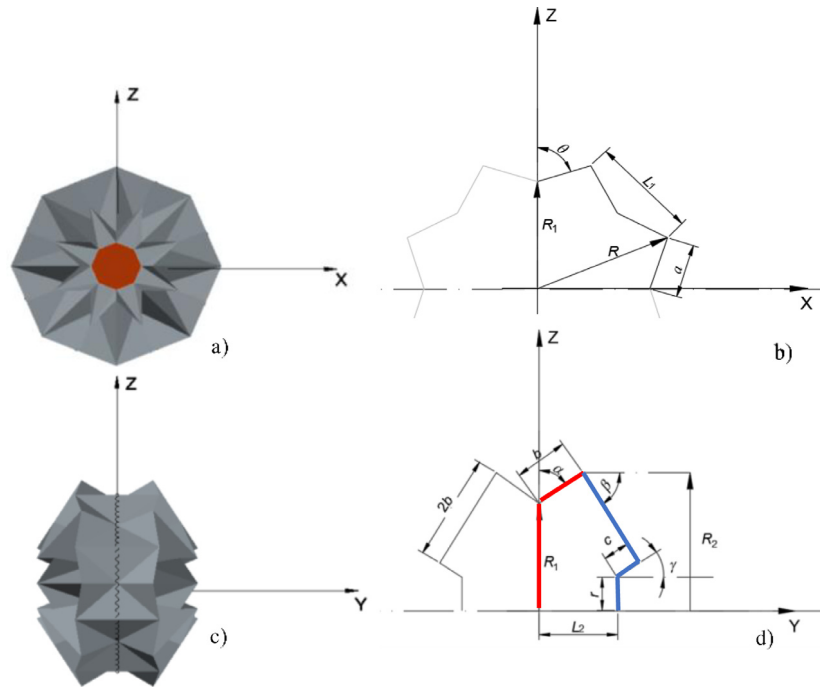$$R = \frac{L_1}{2 \sin \frac{\pi}{8}} \tag{5}$$

Fig. 5. Plan views of the origami wheel for a geometrical study. (a) and (b) has the XZ plan view — radial symmetry; (c) and (d) has the YZ plan view — axial symmetry.
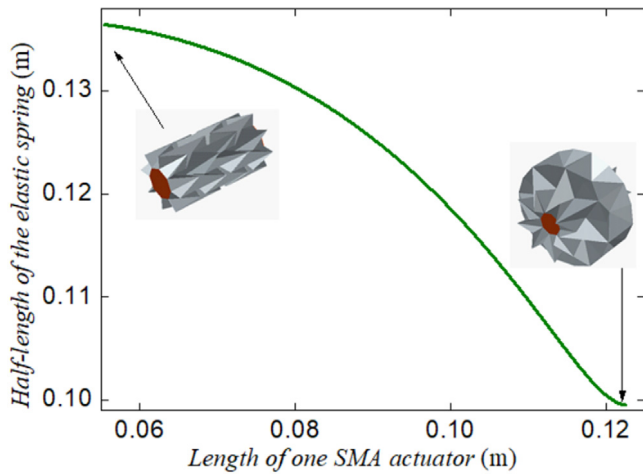

Fig. 6. Geometric description of the origami-wheel opening/closure process.

Besides, it is possible to establish a geometric relation presented in the sequence,

$$\cos(\theta)\cos(\alpha)\tan(\lambda) + |\sin(\alpha)| = 1 \tag{6}$$

Geometric relations can be solved as a function of L_1, the SMA length, represented by the unit cell opening, resulting in an explicit relation $L_2 = f(L_1)$, where L_2 is the half-length of the elastic passive spring. Based on that, the origami wheel can be modeled as a 1-degree of freedom system (1-DOF) and the displacements of the SMAs and the elastic passive spring can be related to each other based on geometrical properties of the origami-wheel (Fig. 6).

4. Origami wheel robot model

This section presents the origami wheel robot mathematical model, considering an independent wheel radius variation and therefore, each one can rotate at different angular speed. The robot movement is described with respect to a fixed observer, F, by the positioning of the G point (X, Y, Z) and the yaw angle (Φ), Fig. 7. These variables can be written as a function of R_A and R_B, the A and B wheels radii, respectively. The reduction of the radius of one wheel promotes the yaw motion of the car, allowing maneuverability. The yaw motion is described by the reference frame C (x_1, y_1, z_1) attached to G point (Fig. 7-a). The roll movement of the car is characterized by a rotation θ (Fig. 7-b), related to the wheel radius' reduction, being described by the reference frame P (x_2, y_2, z_2). The kinematics description of the origami-wheel robot considers a reference frame attached to each wheel: reference frame A (x_3^A, y_3^A, z_3^A), which describes the rotation of the wheel A, and B (x_3^B, y_3^B, z_3^B), which describes the rotation of the wheel B (Fig. 7-c and d respectively). The reference frame A rotates following the point N_A. Similarly, the reference frame B rotates following the point N_B. Under these assumptions, the system kinematics can be described by eight variables: position of the chassis (G) on plane (x, y), yaw angle (Φ), roll angle (θ), wheel radius (R_A, R_B) and wheel rotation (ϕ_A, ϕ_B).

4.1. Kinematics

Kinematics analysis of the robot is developed considering reference frames defined in the previous section (Fig. 7). The transformation matrices among these frames are presented in the sequence considering a general notation $^{S1}T^{S2}(\zeta)$ that maps the transformation from reference frame $S1$ to $S2$, according to a rotation ζ.

$$^{F}T^{C} = \begin{bmatrix} \cos(\Phi) & -\sin(\Phi) & 0 \\ \sin(\Phi) & \cos(\Phi) & 0 \\ 0 & 0 & 1 \end{bmatrix}; \quad ^{C}T^{P} = \begin{bmatrix} 1 & 0 & 0 \\ 0 & \cos(\theta) & \sin(\theta) \\ 0 & -\sin(\theta) & \cos(\theta) \end{bmatrix};$$

$$^{P}T^{A} = \begin{bmatrix} \cos(\phi_A) & 0 & \sin(\phi_A) \\ 0 & 1 & 0 \\ -\sin(\phi_A) & 0 & \cos(\phi_A) \end{bmatrix};$$

$$^{P}T^{B} = \begin{bmatrix} \cos(\phi_B) & 0 & \sin(\phi_B) \\ 0 & 1 & 0 \\ -\sin(\phi_B) & 0 & \cos(\phi_B) \end{bmatrix} \tag{7}$$

Inertial reference frame is denoted by F and therefore quantities described with respect to it are called absolute. Four other mobile
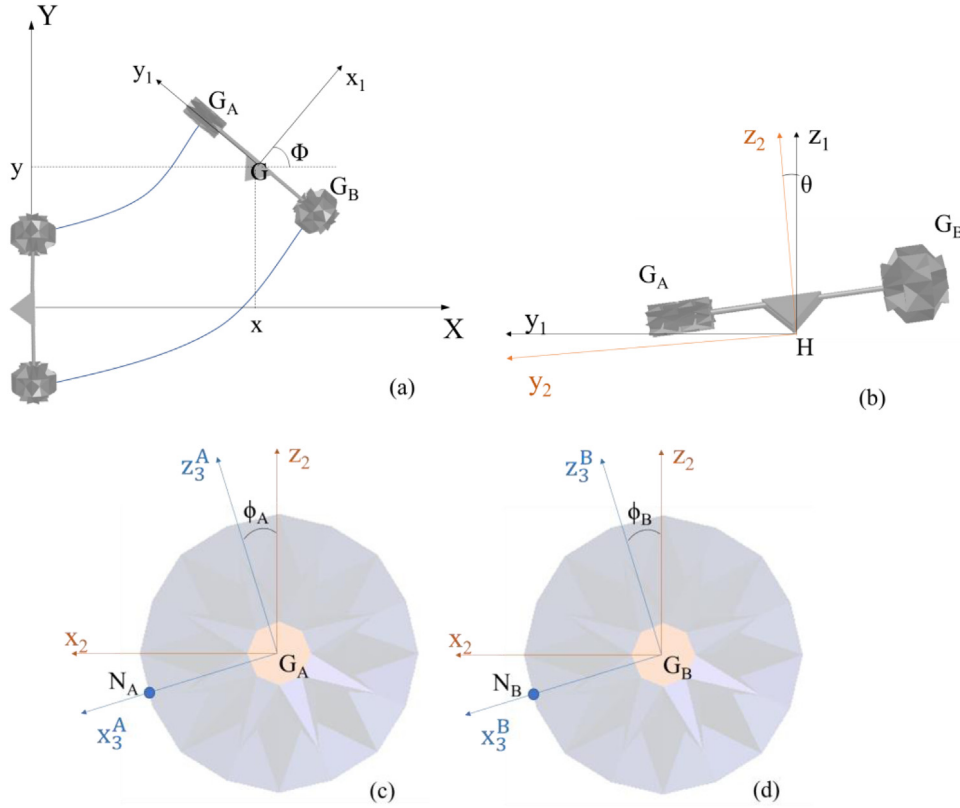
Fig. 7. Representation of the reference frames to describe the origami-wheel trajectory. (a) indication of the yaw motion (Φ); (b) indication of the roll movement (θ); (c) and (d) indication of the reference frame attached to each wheel, for spinning (Φ_A, Φ_B).

reference frames are considered: C, P, A and B. The velocity and position of each mass of the car (wheels and chassis) are described in the reference frame that follows its entity, meaning that is preferable to use the least amount of transformations. Based on that, the chassis is represented in the reference frame P and each wheel is represented at its own reference frame, A or B.

The absolute linear velocity of the chassis, ${}^P v_G$, and the absolute angular velocity of the chassis, ${}^P \omega_P$, are given by

$${}^P v_G = \begin{bmatrix} -\dot{\Phi} R \sin(\theta) + \dot{x} \cos(\Phi) + \dot{y} \sin(\Phi) \\ \dot{\theta} R + \cos(\theta)(\dot{y} \cos(\Phi) - \dot{x} \sin(\Phi)) \\ \dot{R} + \sin(\theta)(\dot{y} \cos(\Phi) - \dot{x} \sin(\Phi)) \end{bmatrix} \quad (8)$$

$${}^P \omega_P = \begin{bmatrix} -\dot{\theta} \\ -\dot{\Phi} \sin(\theta) \\ \dot{\Phi} \cos(\theta) \end{bmatrix} \quad (9)$$

where $R = \frac{(R_A + R_B)}{2}$. Besides, the absolute linear velocity of the center of mass of the wheel, ${}^P v_i$, and the absolute angular velocity of the wheel, ${}^i \omega_i$, are given by

$${}^P v_i = \begin{bmatrix} -\dot{\Phi}(R \sin(\theta) + \rho \cos(\theta)) + \dot{x} \cos(\Phi) + \dot{y} \sin(\Phi) \\ \dot{\theta} R + \cos(\theta)(\dot{y} \cos(\Phi) - \dot{x} \sin(\Phi)) \\ \dot{R} - \rho\dot{\theta} + \sin(\theta)(\dot{y} \cos(\Phi) - \dot{x} \sin(\Phi)) \end{bmatrix} \quad (10)$$

$${}^i \omega_i = \begin{bmatrix} -\dot{\theta} \cos(\phi_i) - \dot{\Phi} \cos(\theta) \sin(\phi_i) \\ \dot{\phi_i} - \dot{\Phi} \sin(\theta) \\ -\dot{\theta} \sin(\phi_i) + \dot{\Phi} \cos(\theta) \cos(\phi_i) \end{bmatrix} \quad (11)$$

where it is assumed for wheel A, $i = A$, $\phi_i = \phi_A$ and $\rho = d$ and for wheel B, $i = B$, $\phi_i = \phi_B$ and $\rho = -d$.

The robot performs a roll movement around the axis x_1, defining the yaw motion, being H the contact point between the chassis and the floor (Fig. 7-b). The absolute linear velocity ${}^C v_H$ is given by,

$${}^C v_H = \begin{bmatrix} \dot{x} \cos(\Phi) + \dot{y} \sin(\Phi) \\ \dot{y} \cos(\Phi) - \dot{x} \sin(\Phi) \\ 0 \end{bmatrix} \quad (12)$$

The velocity of point N_i $i = (A, B)$ is described in the reference frame that follows the wheel rotation. Hence, the velocity of N_i of the wheel i, $i = A, B$, is given by ${}^i v_{N_i} = \begin{bmatrix} v_{x_3} & v_{y_3} & v_{z_3} \end{bmatrix}^T$, where each component is presented in the sequence

$$v_{x_3} = [\dot{x} \cos(\Phi) + \dot{y} \sin(\Phi)] \cos(\phi_i) + [\dot{x} \sin(\Phi) - \dot{y} \cos(\Phi)]$$
$$\times \sin(\theta) \sin(\phi_i) + \dot{R}_i - (\dot{R} + \dot{\theta}\rho) \sin(\phi_i)$$
$$- \dot{\Phi} [\rho \cos(\theta) + R \sin(\theta)] \cos(\phi_i) \quad (13a)$$

$$v_{y_3} = \cos(\theta) \left[-\dot{x} \sin(\Phi) + \dot{y} \cos(\Phi) + \dot{\Phi} R_i \cos(\phi_i) \right] + \dot{\theta} \left[R - R_i \sin(\phi_i) \right] \quad (13b)$$

$$v_{z_3} = [\dot{x} \cos(\Phi) + \dot{y} \sin(\Phi)] \sin(\phi_i) - [\dot{x} \sin(\Phi) - \dot{y} \cos(\Phi)]$$
$$\times \sin(\theta) \cos(\phi_i) + (\dot{R} - \dot{\theta}\rho) \cos(\phi_i) - \dot{\phi_i} R_i$$
$$- \dot{\Phi}\{[\rho \cos(\theta) + R \sin(\theta)] \sin(\phi_i) - R_i \sin(\theta)\} \quad (13c)$$

where $\rho = d$ and $i = A$, for wheel A, and $\rho = -d$ and $i = B$, for wheel B.

4.2. Constraints

The robot movement needs to be associated with constraints in order to be properly described. Five nonslip conditions are described in this formulation: each wheel roll without slipping in the direction of the motion; both wheels maintain contact with the floor during the entire motion, without penetration or jumping; and there is no slide on the contact between the chassis and the soil, represented by the contact point H. The description of these constraints consider that, $\phi_A = \frac{\pi}{2}$ and $\phi_B = \frac{\pi}{2}$; e_{z_3} is the unitary vector on the motion direction, z_3^i ($i = A, B$), and e_{z_1} is the unitary vector on the direction perpendicular to the motion, z_1^C.
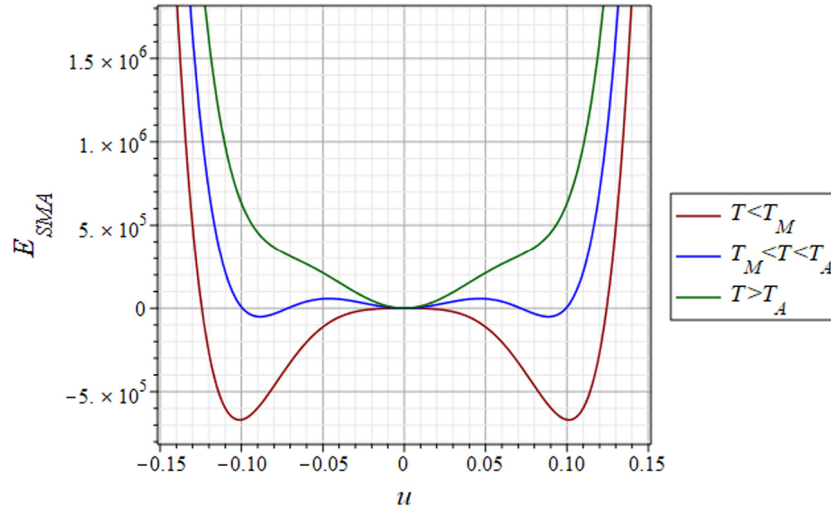
Fig. 8. Potential energy of the polynomial constitutive model.

Considering the first nonslip condition, the velocity of N_i vanishes at the point of contact of each wheel with the soil in the direction of the motion, z_3^i. Therefore, the first nonslip condition is given by $v_{z_3}^i = 0$ at $\phi_i = \frac{\pi}{2}$. Therefore, the constraints are expressed by,

$$v_{z_3}^A = {}^A\boldsymbol{v}_{N_A}\left(\phi_A = \frac{\pi}{2}\right) \cdot \boldsymbol{e}_{z_3} = 0$$
$$v_{z_3}^B = {}^B\boldsymbol{v}_{N_B}\left(\phi_B = \frac{\pi}{2}\right) \cdot \boldsymbol{e}_{z_3} = 0 \qquad (14)$$

Based on these equations, the following constraints are defined,

$$\dot{x}\cos(\Phi) + \dot{y}\sin(\Phi) - \dot{\Phi}[d\cos(\theta) - D\sin(\theta)] = \dot{\phi}_A R_A \qquad (15)$$

$$\dot{x}\cos(\Phi) + \dot{y}\sin(\Phi) + \dot{\Phi}[d\cos(\theta) - D\sin(\theta)] = \dot{\phi}_B R_B \qquad (16)$$

where $D = \frac{R_A - R_B}{2}$.

Next step is to analyze the vertical component of each wheel velocity described on either C or P reference frame. In the contact point of each wheel with the soil, the vertical component of the velocity $\left(v_{z_1}\right)$ vanishes. Therefore,

$$v_{z_1}^A = {}^C\boldsymbol{v}_{N_A}\left(\phi_A = \frac{\pi}{2}\right) \cdot \boldsymbol{e}_{z_1} = 0$$
$$v_{z_1}^B = {}^C\boldsymbol{v}_{N_B}\left(\phi_B = \frac{\pi}{2}\right) \cdot \boldsymbol{e}_{z_1} = 0 \qquad (17)$$

Considering the components described by Eqs. (13a) to (13c) and the transformation matrices (7), the vertical component of the velocity in the contact point $\phi_i = \frac{\pi}{2}$ ($i = A, B$) is given by

$$v_{z_1} = -\dot{\theta}\left[(R - R_i)\sin(\theta) + \rho\cos(\theta)\right] + (\dot{R} - \dot{R}_i)\cos(\theta) \qquad (18)$$

where $\rho = d$ and $i = A$ for wheel A, and $\rho = -d$ and $i = B$, for wheel B. Since $R = \frac{R_A + R_B}{2}$ and $D = \frac{R_A - R_B}{2}$, and imposing the nonslip condition $\left(v_{z_1} = 0\right)$, the third constraint is reduced to a single equation as follows

$$-\dot{\theta}[-D\sin(\theta) + d\cos(\theta)] - \dot{D}\cos(\theta) = 0 \qquad (19)$$

Finally, the last condition considers the contact between the chassis and the soil. Since there is not sliding motion in the direction perpendicular to the motion, the constraint is obtained by imposing that the lateral absolute velocity vanishes,

$$v_{y_1}^H = {}^C\boldsymbol{v}_H \cdot \boldsymbol{e}_{z_1} = 0 \qquad (20)$$

Therefore, based on the previous definitions, this is represented by the following equation

$$\dot{x}\sin(\Phi) - \dot{y}\cos(\Phi) = 0 \qquad (21)$$

Therefore, kinematics is described with 8 variables ($x, y, \Phi, \theta, R_A, R_B, \phi_A, \phi_B$) and 4 constraints (Eq. (14), (15), (16), (17)), resulting in a 4-DOF model.
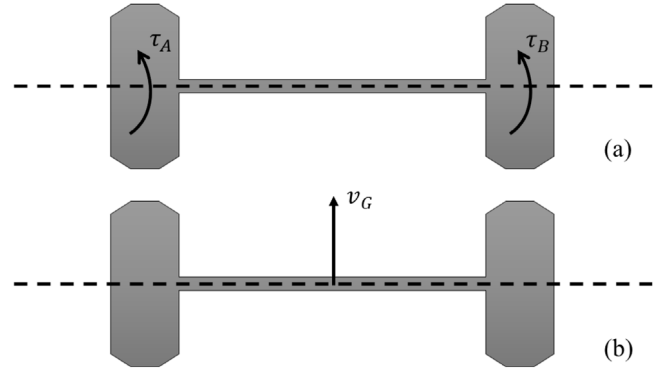

Fig. 9. Driven situations of the robot: (a) driven torques at each wheel; (b) robot linear velocity.

4.3. Equations of motion

The dynamical model of the origami wheel robot is built by energetic approach, considering Lagrange multipliers to represent constraints. The Lagrangian is defined as the difference between the kinetic, E_k, and potential, E_p, energies ($\mathcal{L} = E_k - E_p$), being described as a function of generalized coordinates, $q_i^* = \left[x, y, \Phi, \theta, R_A, R_B, \phi_A, \phi_B\right]^T$,

$$\frac{d}{dt}\left(\frac{\partial \mathcal{L}}{\partial \dot{q}_i^*}\right) - \frac{\partial \mathcal{L}}{\partial q_i^*} = Q_i + \sum_{j=1}^{N-N_0} \lambda_j f_{ij} \quad (i = 1, \ldots, N) \qquad (22)$$

where Q_i are the generalized forces, N is the number of variables that describe the system, N_0 is the number of degrees of freedom, λ_j are the Lagrange multipliers and f_{ij} are the multiplier factors for the constraint equation.

Non-holonomic constraints defined in the previous section are expressed by the following equations. The multiplier factors for the Lagrange equation are obtained by comparing Eq. (23) with each one of the constraints (Eqs. (15), (16), (19) and (21)), expressed in Table 1.

$$\sum_{j=1}^{N} f_{ij}\delta q_i^* = 0 \quad (i = 1, \ldots, N - N_0) \qquad (23)$$

The kinetic energy can be divided into translational, E_k^T, and rotational E_k^R energies, presented in the sequence,

$$E_k^T = \frac{m_t}{2}\left\{\dot{x}^2 + \dot{y}^2 + \dot{R}^2 - 2\dot{\Phi}\dot{R}\sin(\theta)\left[\dot{x}\cos(\Phi) + \dot{y}\sin(\Phi)\right]\right.$$
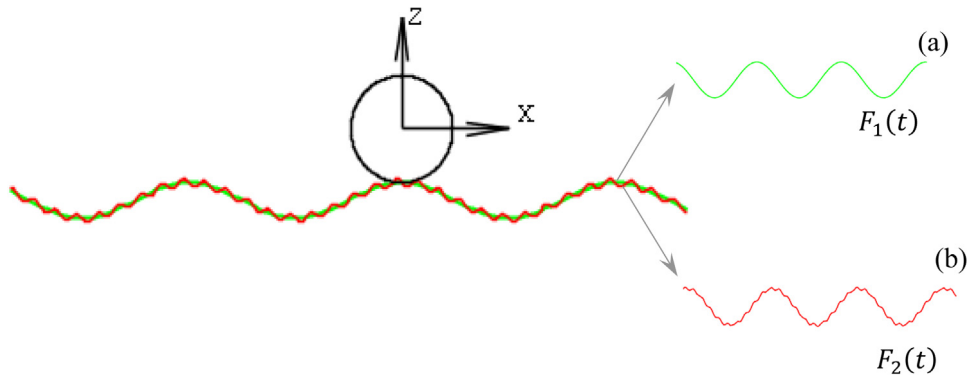
Fig. 10. Representation of the external excitation represented by the force $F(t) = F_1(t) + F_2(t)$, where the contribution of each $F_i(t)$ is highlighted on the right, being (a) for $F_1(t)$ and (b) for $F_2(t)$.
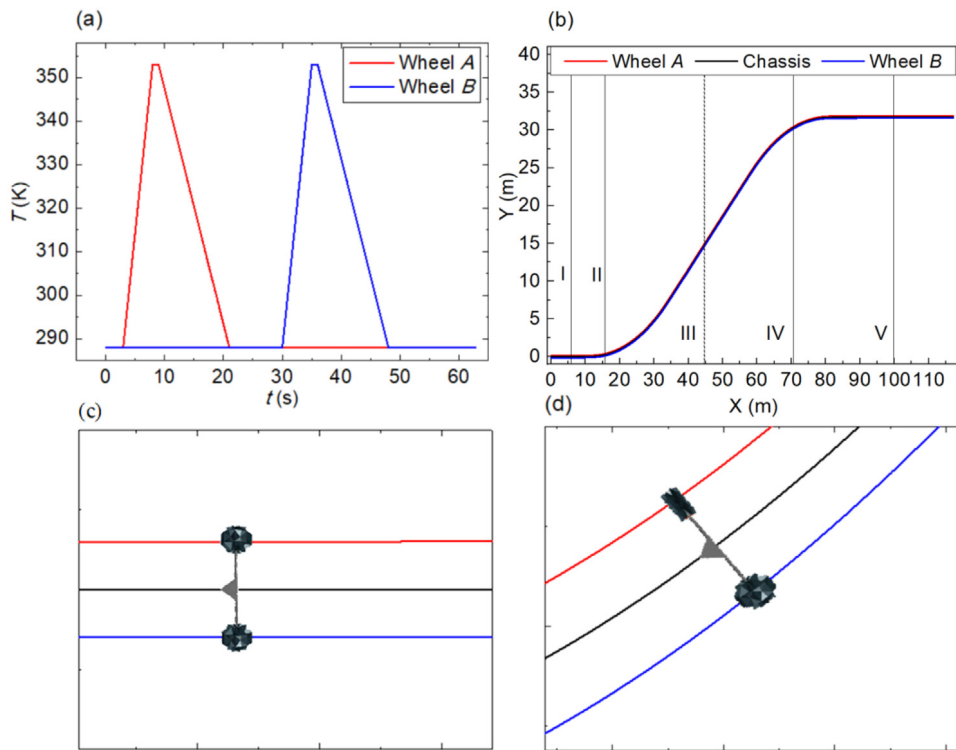

Fig. 11. Representation for an arbitrary desired path of the origami wheel robot. (a) Thermal load applied to each wheel individually, promoting a turn counterclockwise and then clockwise; (b) desired arbitrary path, starting with a straight line and ending on a straight line, shifted vertically from the original one; (c) zoom on the region I pointed at (b), where the car follows a straight line; (d) zoom on the region II, where the car turns left (counterclockwise turn from wheel B to wheel A).

Table 1
Multiplier factors for the constraint equations associated with each Lagrange multiplier.

f_{ij}	$j = 1$	$j = 2$	$j = 3$	$j = 4$
$i = 1$	$\cos(\Phi)$	$\cos(\Phi)$	0	$\sin(\Phi)$
$i = 2$	$\sin(\Phi)$	$\sin(\Phi)$	0	$-\cos(\Phi)$
$i = 3$	$D\sin(\theta) - d\cos(\theta)$	$d\cos(\theta) - D\sin(\theta)$	0	0
$i = 4$	0	0	$d\cos(\theta) - D\sin(\theta)$	0
$i = 5$	0	0	$\cos(\theta)/2$	0
$i = 6$	0	0	$-\cos(\theta)/2$	0
$i = 7$	$-R_A$	0	0	0
$i = 8$	0	$-R_B$	0	0

$$+ \left[\dot{\Phi}^2 \sin^2(\theta) + \dot{\theta}^2\right] R^2$$

$$+ 2\left[\dot{\theta}R\cos(\theta) + \dot{R}\sin(\theta)\right]\left[\dot{y}\cos(\Phi) - \dot{x}\sin(\Phi)\right]\}$$

$$+ \left[\frac{(m_t - m_G)d^2}{2} + M\left(f_A^2 + f_B^2\right)\right]\left[\dot{\Phi}^2\cos^2(\theta) + \dot{\theta}^2\right]$$

$$+ M\left(\dot{f}_A^2 + \dot{f}_B^2\right) \tag{24}$$

$$E_k^R = \frac{\dot{\theta}^2}{2}\left(I_1^A + I_1^B + J_1\right) - \dot{\Phi}\sin(\theta)\left(\frac{\dot{\phi}_A I_2^A}{2} + \frac{\dot{\phi}_B I_2^B}{2}\right)$$

$$+ \frac{\dot{\Phi}^2}{2}\left[\left(I_1^A + I_1^B + J_3\right)\cos^2(\theta) + \left(I_2^A + I_2^B + J_2\right)\cos^2(\theta)\right] \tag{25}$$

where m_G is the mass of the chassis, M is the mass of each acrylic plate and m_t is the total mass of robot, including chassis and wheels; I_1^i, I_2^i and I_3^i are the principal inertia moments of the origami wheel ($i = A, B$) related to the axis x_3^i, y_3^i and z_3^i, correspondingly; and J_1, J_2 and J_3 are
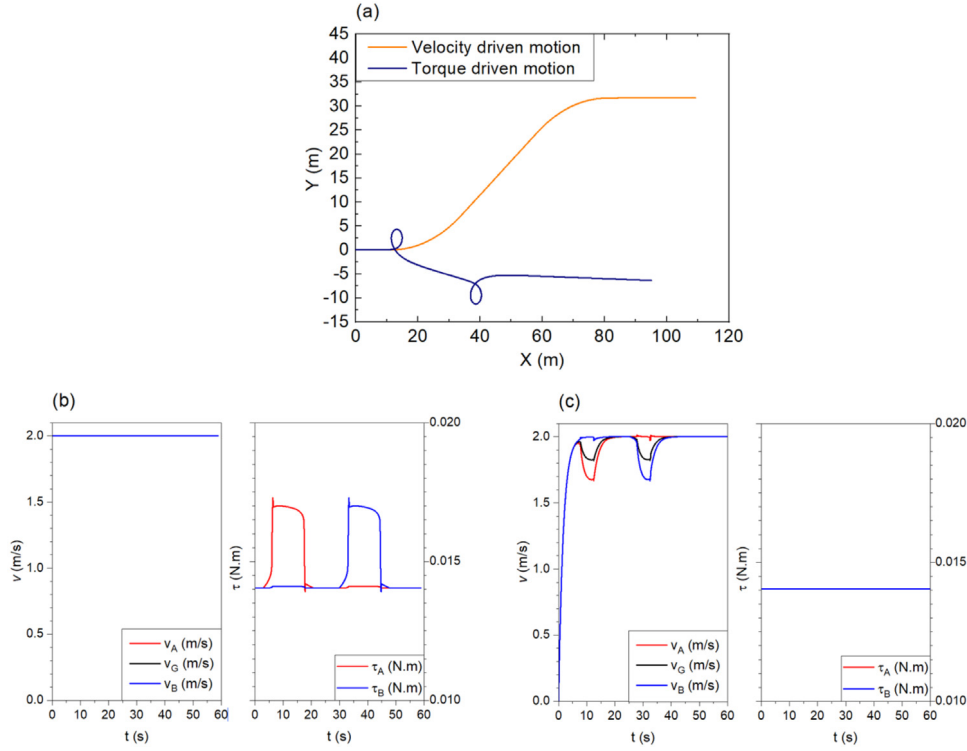
Fig. 12. Origami wheel robot movement for different driven conditions. (a) Path; (b) velocity driven motion: time evolution of the velocities of the chassis and wheels and time evolution of the torques; (c) torque driven motion: time evolution of the linear velocities of the chassis and wheels and time evolution of the torques.

the principal inertia moments of the chassis related to the axis x_2, y_2 and z_2, correspondingly.

The potential energy of the system is a function of the potential energy of actuators (SMAs and elastic passive spring) and the gravitational energy, being expressed as,

$$E_p = E_{SMA_A} + E_{SMA_B} + E_{E_A} + E_{E_B} + m_t g R \cos(\theta) \qquad (26)$$

The expressions for E_{SMA} and E_E depend on the constitutive models. It is adopted that the elastic spring presents linear elastic behavior and the SMA is described by the polynomial constitutive model proposed by Falk [16]. This one-dimensional model assumes a temperature dependent sixth order polynomial free energy $E_{SMA}(\varepsilon, T)$ where ε is the strain and T is the SMA temperature. Based on this potential energy for an SMA sample, it is possible to define an analogous expression for an SMA spring, employed as actuator. Aguiar et al. [17] showed that similar expression $E_{SMA}(u, T)$, where u is the displacement, can be obtained assuming a homogeneous phase transformation on the SMA wire. Therefore, constitutive coefficients are replaced for new parameters that depend on the SMA the spring diameter, D_S, the number of spirals, N_S, and the diameter of the SMA wire, d_S. Based on that, three macroscopic phases are treated: austenite, A, stable at elevated temperatures, and two variants of the martensite, M^+ and M^-, induced by tension and compression, respectively. The sixth-order polynomial free energy is such that at high temperatures, the free energy has only one minimum at vanishing strain; and at low temperatures, it has two minima at non-vanishing strains and a maximum at the vanishing strain (Fig. 8).

$$E_{SMA} = E_{SMA}(u, t) = \frac{\bar{c}_1 (T - T_M) u^2}{2} - \frac{\bar{c}_2 u^4}{4} + \frac{\bar{c}_3 u^6}{6} \qquad (27)$$

where T_M is the temperature below which martensite is stable and $\bar{c}_i$ are defined as follows: $\bar{c}_1 = c_1 \left(\frac{d_S}{\pi D_S^2 N_S} \right)^2$, $\bar{c}_2 = c_2 \left(\frac{d_S}{\pi D_S^2 N_S} \right)^4$ and $\bar{c}_3 = c_3 \left(\frac{d_S}{\pi D_S^2 N_S} \right)^6$, where c_i ($i = 1, 2, 3$) are constitutive model parameters. Another important parameter is the temperature T_A that defines the region where the energy curve has only one minimum, representing the temperature above which only austenitic phase is stable on a stress-free state.

The passive bias actuator is considered to be a linear elastic with a quadratic energy, expressed by the following equation

$$E_E = \frac{k u^2}{2} \qquad (28)$$

where $k = \frac{G_E d_E}{\pi D_E^2 N_E}$ is the stiffness defined by the spring diameter, D_E, the wire diameter, d_E, the number of spirals, N_E, and the tangent coefficient of the material component of the spring, G_E.

By employing the Lagrange equation (22), considering the constraints expressed in Table 1, and the non-conservative forces acting on the system, it is possible to obtain the following equations. Note that external forces applied to the wheels are represented by $F_A(t)$ and $F_B(t)$, ξ is the viscous damping coefficient that represents the general dissipation of the system that includes the SMA and other kinds of dissipation associated to the folding process of the origami-wheel. The dissipation related to the wheel rolling motion is represented by the viscous damping coefficient, ξ_w, associated with any dissipation of the wheel, being related to the angular velocity of the wheels; τ_A and τ_B are the torques acting on each wheel.
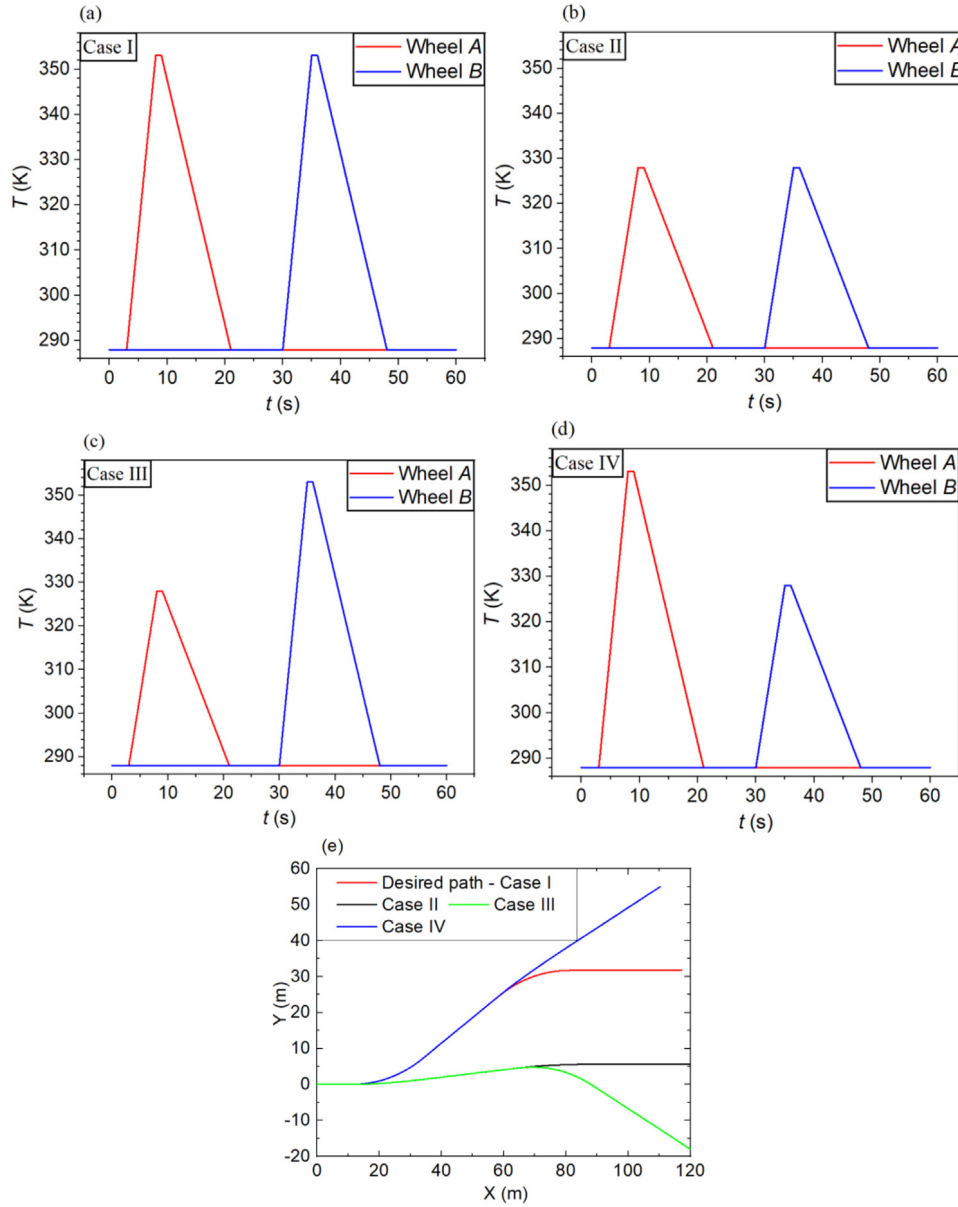
Fig. 13. Thermal cycles (a – d) and path (e) described by the projection of G point on the fixed frame (X,Y,Z).

$$\frac{d}{dt}\left(\frac{\partial \mathfrak{L}}{\partial \dot{q}_1^*}\right) - \frac{\partial \mathfrak{L}}{\partial q_1^*} = \lambda_1 \cos(\Phi) + \lambda_2 \cos(\Phi) + \lambda_4 \sin(\Phi)$$

$$\frac{d}{dt}\left(\frac{\partial \mathfrak{L}}{\partial \dot{q}_2^*}\right) - \frac{\partial \mathfrak{L}}{\partial q_2^*} = \lambda_1 \sin(\Phi) + \lambda_2 \sin(\Phi) - \lambda_4 \cos(\Phi)$$

$$\frac{d}{dt}\left(\frac{\partial \mathfrak{L}}{\partial \dot{q}_3^*}\right) - \frac{\partial \mathfrak{L}}{\partial q_3^*} = (\lambda_1 - \lambda_2)\left[D \sin(\theta) - d \cos(\theta)\right]$$

$$\frac{d}{dt}\left(\frac{\partial \mathfrak{L}}{\partial \dot{q}_4^*}\right) - \frac{\partial \mathfrak{L}}{\partial q_4^*} = -\lambda_3\left[D \sin(\theta) - d \cos(\theta)\right]$$

$$\frac{d}{dt}\left(\frac{\partial \mathfrak{L}}{\partial \dot{q}_5^*}\right) - \frac{\partial \mathfrak{L}}{\partial q_5^*} = F_A(t) - \xi \dot{R}_A + \lambda_3 \frac{\cos(\theta)}{2}$$

$$\frac{d}{dt}\left(\frac{\partial \mathfrak{L}}{\partial \dot{q}_6^*}\right) - \frac{\partial \mathfrak{L}}{\partial q_6^*} = F_B(t) - \xi \dot{R}_B - \lambda_3 \frac{\cos(\theta)}{2}$$

$$\frac{d}{dt}\left(\frac{\partial \mathfrak{L}}{\partial \dot{q}_7^*}\right) - \frac{\partial \mathfrak{L}}{\partial q_7^*} = \tau_A - \xi_w \dot{\phi}_A - R_A \lambda_1$$

$$\frac{d}{dt}\left(\frac{\partial \mathfrak{L}}{\partial \dot{q}_8^*}\right) - \frac{\partial \mathfrak{L}}{\partial q_8^*} = \tau_B - \xi_w \dot{\phi}_B - R_B \lambda_2$$

(29)

Eliminating the Lagrange multipliers of the set of Eqs. (29), four equations of motion describe the origami robot movement

$$\left(\frac{d}{dt}\left(\frac{\partial \mathfrak{L}}{\partial \dot{q}_1^*}\right) - \frac{\partial \mathfrak{L}}{\partial q_1^*}\right)\cos(\Phi) + \left(\frac{d}{dt}\left(\frac{\partial \mathfrak{L}}{\partial \dot{q}_2^*}\right) - \frac{\partial \mathfrak{L}}{\partial q_2^*}\right)\sin(\Phi)$$

$$= \frac{\tau_A - \xi_w \dot{\phi}_A - \left(\frac{d}{dt}\left(\frac{\partial \mathfrak{L}}{\partial \dot{q}_7^*}\right) - \frac{\partial \mathfrak{L}}{\partial q_7^*}\right)}{R_A} + \frac{\tau_B - \xi_w \dot{\phi}_B - \left(\frac{d}{dt}\left(\frac{\partial \mathfrak{L}}{\partial \dot{q}_8^*}\right) - \frac{\partial \mathfrak{L}}{\partial q_8^*}\right)}{R_B}$$

$$\frac{d}{dt}\left(\frac{\partial \mathfrak{L}}{\partial \dot{q}_3^*}\right) - \frac{\partial \mathfrak{L}}{\partial q_3^*}$$

$$= \left(\frac{\tau_A - \xi_w \dot{\phi}_A - \left(\frac{d}{dt}\left(\frac{\partial \mathfrak{L}}{\partial \dot{q}_7^*}\right) - \frac{\partial \mathfrak{L}}{\partial q_7^*}\right)}{R_A} - \frac{\tau_B - \xi_w \dot{\phi}_B - \left(\frac{d}{dt}\left(\frac{\partial \mathfrak{L}}{\partial \dot{q}_8^*}\right) - \frac{\partial \mathfrak{L}}{\partial q_8^*}\right)}{R_B}\right)$$

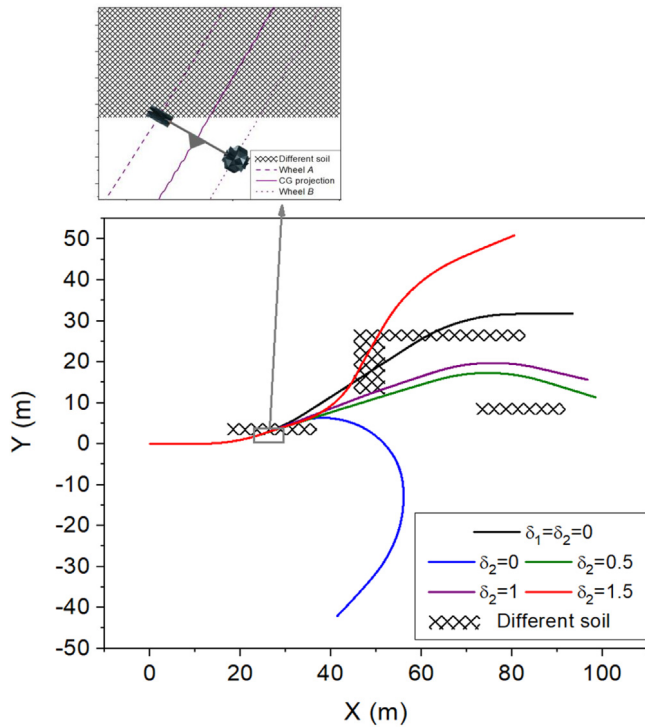$$\times \left[D \sin(\theta) - d \cos(\theta)\right]$$

Fig. 14. Path followed by the origami-wheel robot when passing through different soils, represented by hatched regions and described by an external stimulus. A zoom from the first dashed regions is also presented.

$$\frac{d}{dt}\left(\frac{\partial \mathcal{L}}{\partial \dot{q}_5^*}\right) - \frac{\partial \mathcal{L}}{\partial q_5^*} = F_A(t) - \xi \dot{R}_A - \frac{\frac{d}{dt}\left(\frac{\partial \mathcal{L}}{\partial \dot{q}_4^*}\right) - \frac{\partial \mathcal{L}}{\partial q_4^*}}{D \sin(\theta) - d \cos(\theta)} \frac{\cos(\theta)}{2}$$

$$\frac{d}{dt}\left(\frac{\partial \mathcal{L}}{\partial \dot{q}_6^*}\right) - \frac{\partial \mathcal{L}}{\partial q_6^*} = F_B(t) - \xi \dot{R}_B + \frac{\frac{d}{dt}\left(\frac{\partial \mathcal{L}}{\partial \dot{q}_4^*}\right) - \frac{\partial \mathcal{L}}{\partial q_4^*}}{D \sin(\theta) - d \cos(\theta)} \frac{\cos(\theta)}{2}$$

(30)

Equations of motion can be rewritten in matrix form as follows,

$$\boldsymbol{M}(\boldsymbol{q})\ddot{\boldsymbol{q}} + \boldsymbol{C}(\dot{\boldsymbol{q}}, \boldsymbol{q})\dot{\boldsymbol{q}} + \boldsymbol{D}(\boldsymbol{q})\dot{\boldsymbol{q}} + \boldsymbol{g}(\boldsymbol{q}) = \boldsymbol{f}_{ext} \qquad (31)$$

where $\boldsymbol{q} = \left[x, \Phi, R_A, R_B\right]^T$ is the independent generalized coordinate vector, $\boldsymbol{M}(\boldsymbol{q})$ is the inertia matrix, $\boldsymbol{C}(\dot{\boldsymbol{q}}, \boldsymbol{q})$ is the matrix containing the higher-order terms on $\dot{\boldsymbol{q}}$, $\boldsymbol{D}(\boldsymbol{q})$ is the damping matrix, $\boldsymbol{g}(\boldsymbol{q})$ is the stiffness and gravitational vector and $\boldsymbol{f}_{ext}$ is the vector with the external forces. The inertia matrix is composed by terms that evolve on time with the form

$$\boldsymbol{M}(\boldsymbol{q}) = \begin{bmatrix} m_{11} & m_{12} & 0 & 0 \\ m_{21} & m_{22} & 0 & 0 \\ 0 & 0 & m_{33} & m_{34} \\ 0 & 0 & m_{34} & m_{44} \end{bmatrix} \qquad (32)$$

with determinant $\det(\boldsymbol{M}(\boldsymbol{q})) = \left(m_{11}m_{22} - m_{12}m_{21}\right)\left(m_{33}m_{44} - m_{34}^2\right)$.

Since its determinant is always non-zero, it is possible to invert the inertia matrix, resulting in the following equation.

$$\ddot{\boldsymbol{q}} = \boldsymbol{M}^{-1}(\boldsymbol{q})\left[\boldsymbol{f}_{ext} - \boldsymbol{C}(\dot{\boldsymbol{q}}, \boldsymbol{q})\dot{\boldsymbol{q}} - \boldsymbol{D}(\boldsymbol{q})\dot{\boldsymbol{q}} - \boldsymbol{g}(\boldsymbol{q})\right] \qquad (33)$$

This equation of motion is solved using a fourth order Runge–Kutta method with fixed steps using the equation in its canonical form.
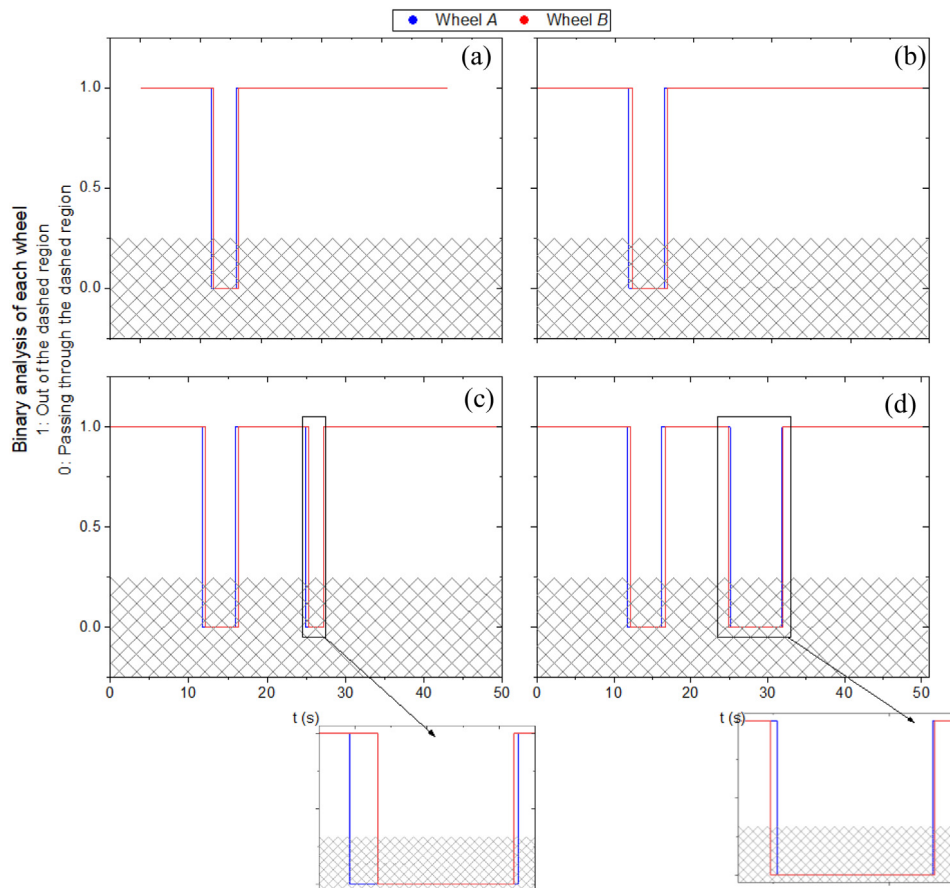

Fig. 15. Binary representation of the wheels related to the dashed region in Fig. 14.. (For interpretation of the references to color in this figure legend, the reader is referred to the web version of this article.)
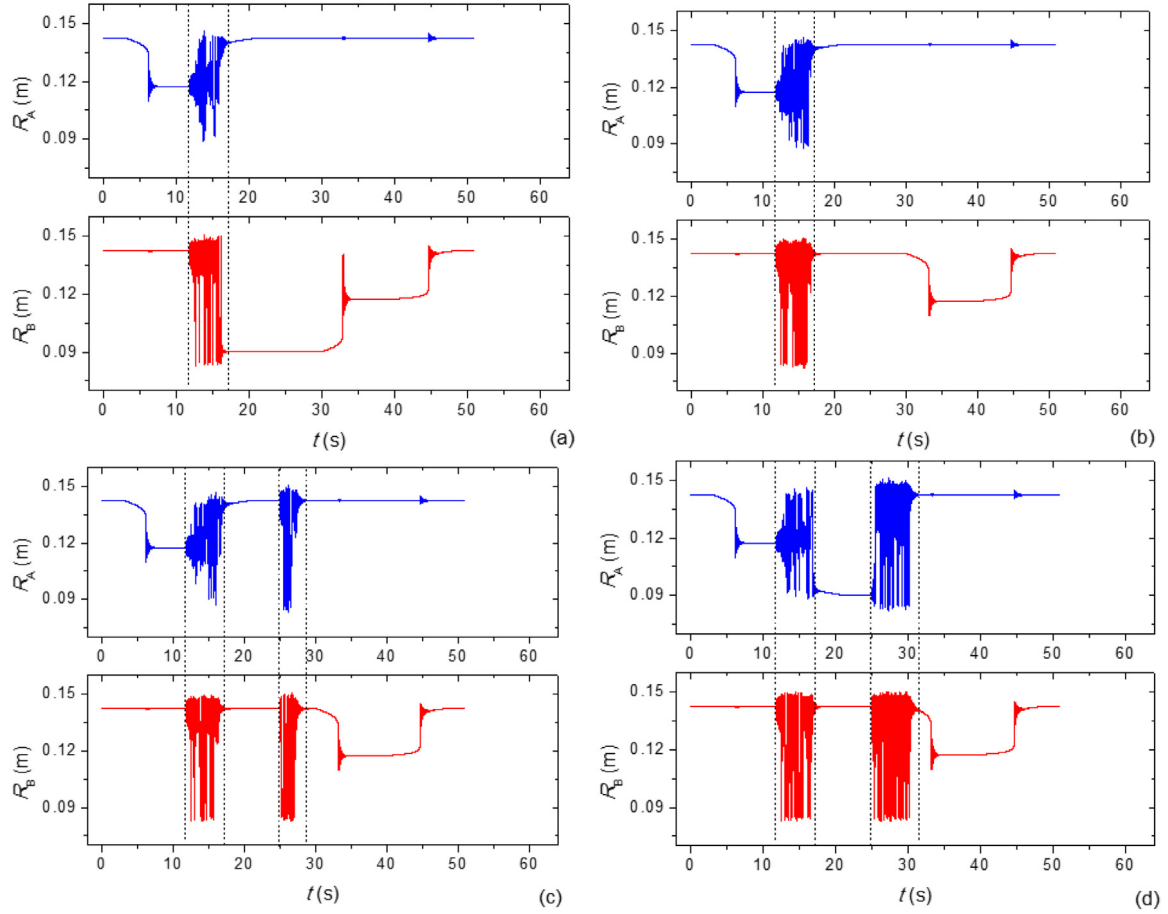
Fig. 16. Time evolution of the wheels' radius for the cases (a) $\delta_2 = 0N$; (b) $\delta_2 = 0.5N$; (c) $\delta_2 = 1N$ and (d) $\delta_2 = 1.5N$.

4.4. Different driven cases

The movement of the robot is driven by the motors attached to each one of the wheels, described by a torque τ_i $(i = A, B)$. Alternatively, the motion can be driven by the robot linear velocity, instead of prescribing the torques. The two driving possibilities are represented in Fig. 9.

Based on that, consider a situation where the torques are prescribed. The resistance to rotation is assumed to be the same for both wheels, being represented by $\xi_w \dot{\phi}_i$. In this regard, the torque driven motion of the robot has the following velocity,

$$v_G = \frac{v_A + v_B}{2} = \frac{\tau_A R_A}{2\xi_w} + \frac{\tau_B R_B}{2\xi_w} \tag{34}$$

Alternatively, by considering a motion driven by the robot linear velocity, since the wheels radius change, the linear velocity is a function of the angular velocity of the wheel and the radius rate variation, given by

$$v_i = \dot{\phi}_i R_i + \phi_i \dot{R}_i \quad (i = A \text{ or } B) \tag{35}$$

By considering the dynamic equilibrium of a single wheel under rotation, the torques τ_A and τ_B are obtained as follows: $\tau_i - \xi_w \dot{\phi}_i = I_i \ddot{\phi}_i$ $(i = A \text{ or } B)$. By calculating $\dot{\phi}_i$ and $\ddot{\phi}_i$ from kinematics argues, the following equation is obtained,

$$\tau_i = -\frac{I_i}{R_i} \phi_i \ddot{R}_i - 2\frac{I_i}{R_i} \dot{\phi}_i \dot{R}_i - \frac{\phi_i \xi_w}{R_i} \dot{R}_i + \xi_w \frac{v_G}{R_i} \quad (i = A \text{ or } B) \tag{36}$$

4.5. External forcing

The origami–soil interaction is a difficult problem to be described. The essence of the interaction is the nonlinearity in contact mechanics,

where the contact reaction and contact surface can only be specified after contact [3]. Usually, the wheel–soil interaction takes into account the contact area between the wheel and the soil, the wheel flexibility, soil malleability and wheel sinkage [18]. Flexible wheels, however, require a modified study of the pressure-sinkage models, once that the wheel flexibility might lead to larger sinkage areas when comparing a rigid and a flexible wheel with same radius [19–21]. A simplified description of origami wheel–soil interaction can be represented by an external mechanical stimulus represented by an external force. In this regard, soil interaction can be described by different harmonic excitations, representing the main excitation and the soil roughness, for instance. Dissipative aspects are represented by the general term presented in the previous subsection. This approach allows one to exploit deviations of the robot desired path. Hence, for the sake of simplicity, it is adopted an external stimulus represented by two terms: $F(t) = F_1(t) + F_2(t)$, where $F_1(t) = \delta_1 \sin(\omega_1 t)$ and $F_2(t) = \delta_2 \sin(\omega_2 t)$.

The term $\delta_1 \sin(\omega_1 t)$ represents different forms of the soil (sinusoid, for instance - Fig. 10 a). On the other hand, the second term, $\delta_2 \sin(\omega_2 t)$, represents a perturbation over the original soil (Fig. 10 b).

5. Numerical simulations

Numerical simulations of the origami wheel robot are carried out considering system parameters presented in Table 2 that presents constitutive and actuator parameters together with the robot construction characteristics.

Initially, consider a situation where the motion is driven by a constant linear velocity $|v_G| = 2$ m/s, associated with torque values $\tau_A = \tau_B = 0.0141$ Nm and $\xi_w = 0.001$ Nms/rad. The path changes are defined from wheel radius variations. During the first part of the path,
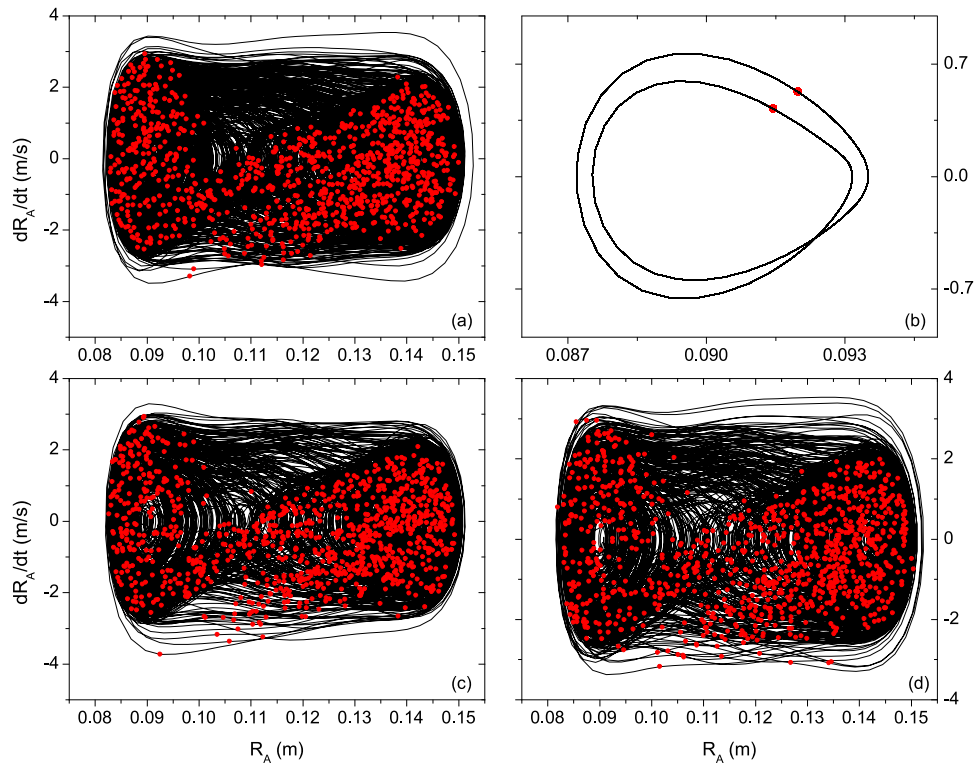
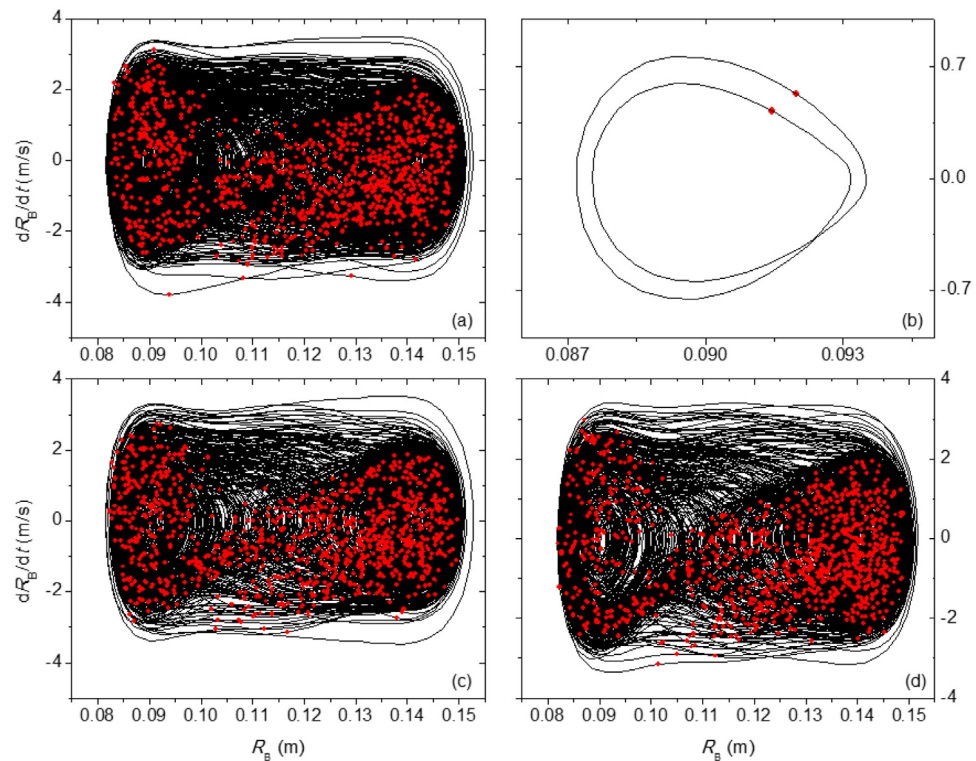**Fig. 17.** Phase portrait and Poincaré section of wheel A for $m_G = 0.1$ kg subjected to F(t) for the cases (a) $\delta_2 = 0N$; (b) $\delta_2 = 0.5N$; (c) $\delta_2 = 1N$ and (d) $\delta_2 = 1.5N$.

Fig. 18. Phase portrait and Poincare section of wheel B for $m_G = 0.1$ kg subjected to F(t) for the cases (a) $\delta_2 = 0$ N; (b) $\delta_2 = 0.5$ N; (c) $\delta_2 = 1$ N and (d) $\delta_2 = 1.5$ N.

the robot is moving forward. A heating/cooling cycle is then applied to the wheel *A*. During the heating process, the SMA recovers its residual displacement, reducing the wheel radius, promoting a path change of the robot to the left (counterclockwise rotation — excerpt II). When it is cooled, the elastic spring induces a displacement similar to the initial

one, recovering the original origami shape. Since both radii are the same, the car returns to a straight path (excerpt III). The same process is then applied to the wheel *B*, turning the origami car to the right (clockwise rotation — excerpt IV), and putting it back to a straight path (excerpt V) on a subsequent cooling process. Fig. 11 shows the robot
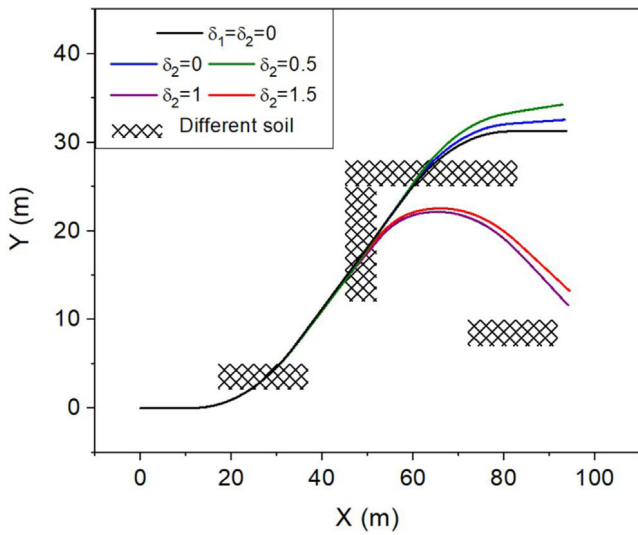
Fig. 19. Path followed by the origami-wheel robot when passing through different soils considering $m_G = 0.2$ kg.

Table 2
Constitutive, mechanical and geometric parameters.

Inertial terms	m_G (kg)	m_t (kg)	M (kg)	
	0.1	0.164	0.012	
Polynomial model	c_1 (MPa/K)	c_2 (MPa)	c_3 (MPa)	
	5	7.0×10^4	7.0×10^6	
Elastic spring	d_E (m)	N_E	G_E (GPa)	D_E (m)
	2.0×10^{-3}	40	30.0	30.0×10^{-3}
SMA spring	d_s (m)	N_s	D_s (m)	T_M (K)	T_A (K)
	1.0×10^{-3}	10	2.5×10^{-3}	291.4	326.4

cooling process, which makes the final excerpt (V) and the first one (I) parallel to each other.

Fig. 12 presents a comparison between the velocity driven and torque driven cases, considering the same temperature changes presented in Fig. 11. Fig. 12-a presents both paths followed by the origami robot, showing dramatic differences. During the heating/cooling process, each wheel individually reduces/increases its radius, promoting a change on the origami robot velocity. Note that the velocity driven case is associated with torques that change their values during the heating/cooling process. The torque of the wheel under the temperature variation increases its value to compensate the radius reduction, keeping the velocity constant at 2 m/s. Once the SMA is cooled down and the initial shape is restored, the torque goes back to the initial value of 0.0141 Nm, as can be seen at Fig. 12-b. On the other hand, for the torque driven case, a reduction on the wheel radius results on a reduction of the wheel velocity to compensate it and keep the torque constant (Fig. 12-c).

From now on, all simulations are performed considering the velocity driven case with $|v_G| = 2$ m/s. Different thermal loads are investigated,
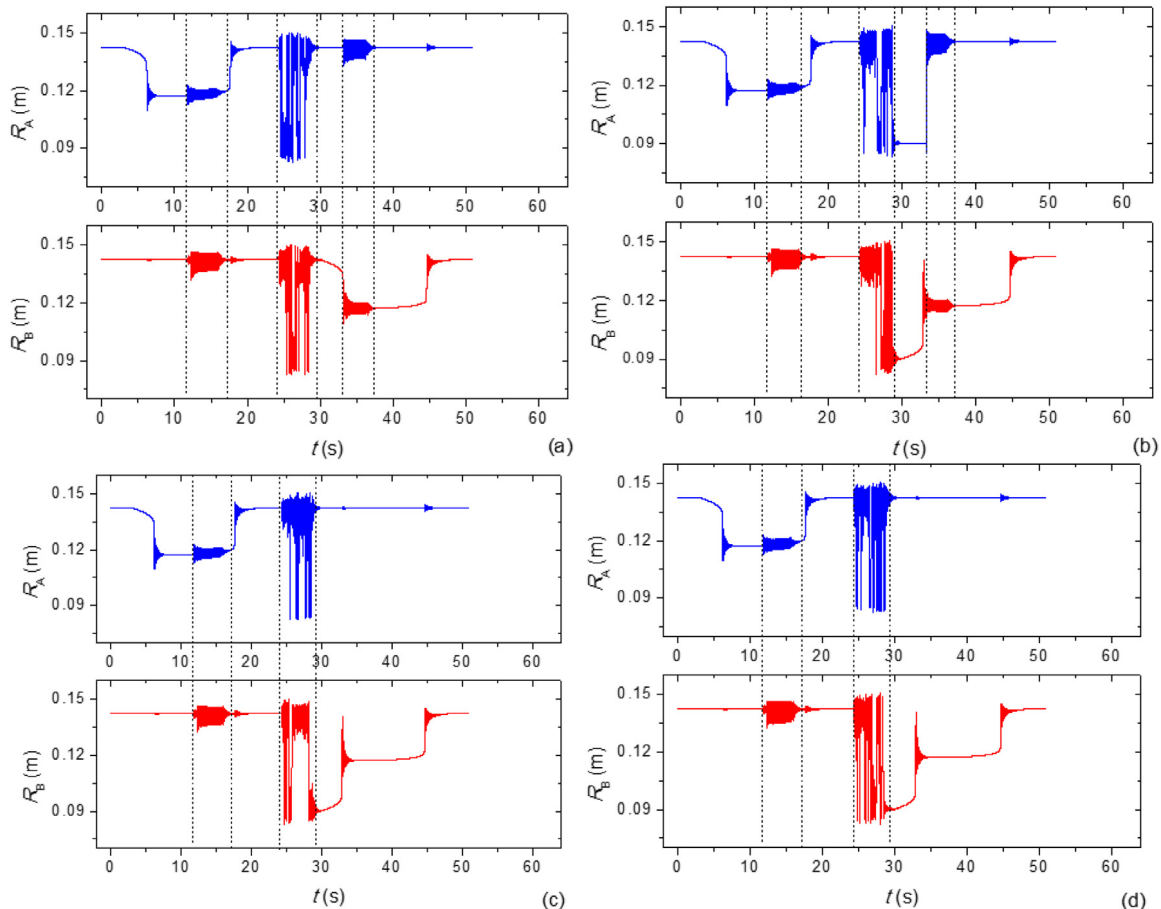
behavior. Fig. 11-a presents the thermal cycles applied to the wheels; Fig. 11-b shows the path followed by the origami robot and Fig. 11-c and Fig. 11-d show zooms at the excerpt I and II, respectively. Note that both heating/cooling cycles have the same rate, and the phase transformation martensite–austenite is completed during the heating process and the reverse austenite–martensite is completed during the

Fig. 20. Time evolution of the wheels' radius considering $m_G = 0.2$ kg for the cases: (a) $\delta_2 = 0N$; (b) $\delta_2 = 0.5N$; (c) $\delta_2 = 1N$ and (d) $\delta_2 = 1.5N$.
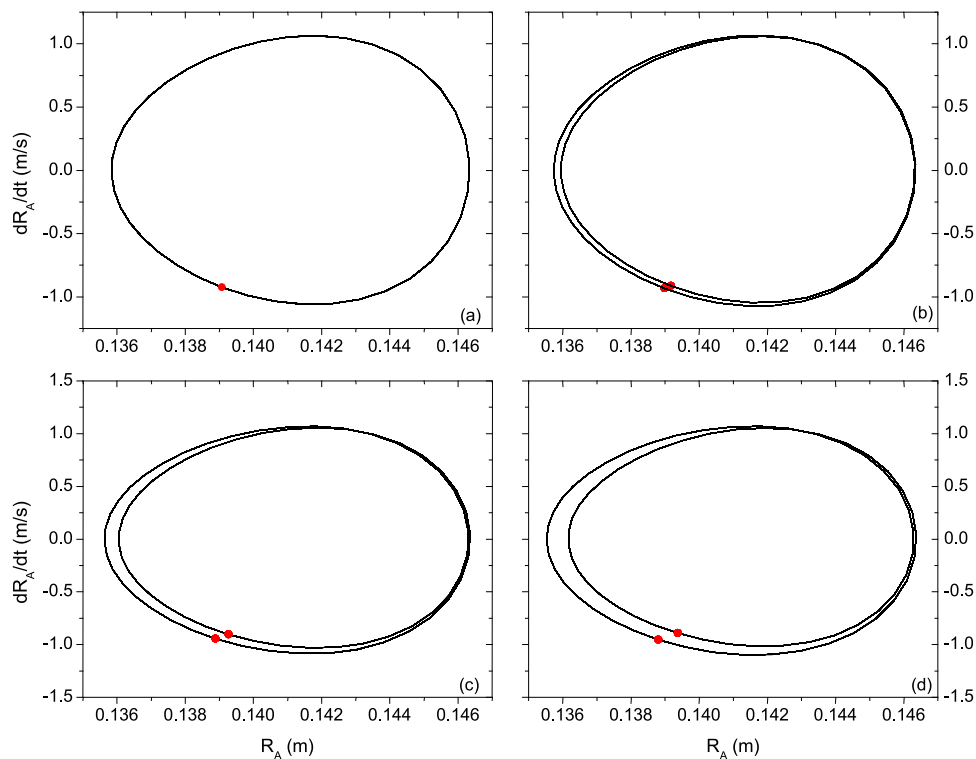
Fig. 21. Phase portrait and Poincare section of wheel A considering $m_G = 0.2$ kg for the cases: (a) $\delta_2 = 0$ N; (b) $\delta_2 = 0.5$ N; (c) $\delta_2 = 1$ N and (d) $\delta_2 = 1.5$ N.

Fig. 22. Phase portrait and Poincare section of wheel B considering $m_G = 0.2$ kg for the cases: (a) $\delta_2 = 0$ N; (b) $\delta_2 = 0.5$ N; (c) $\delta_2 = 1$ N and (d) $\delta_2 = 1.5$ N.
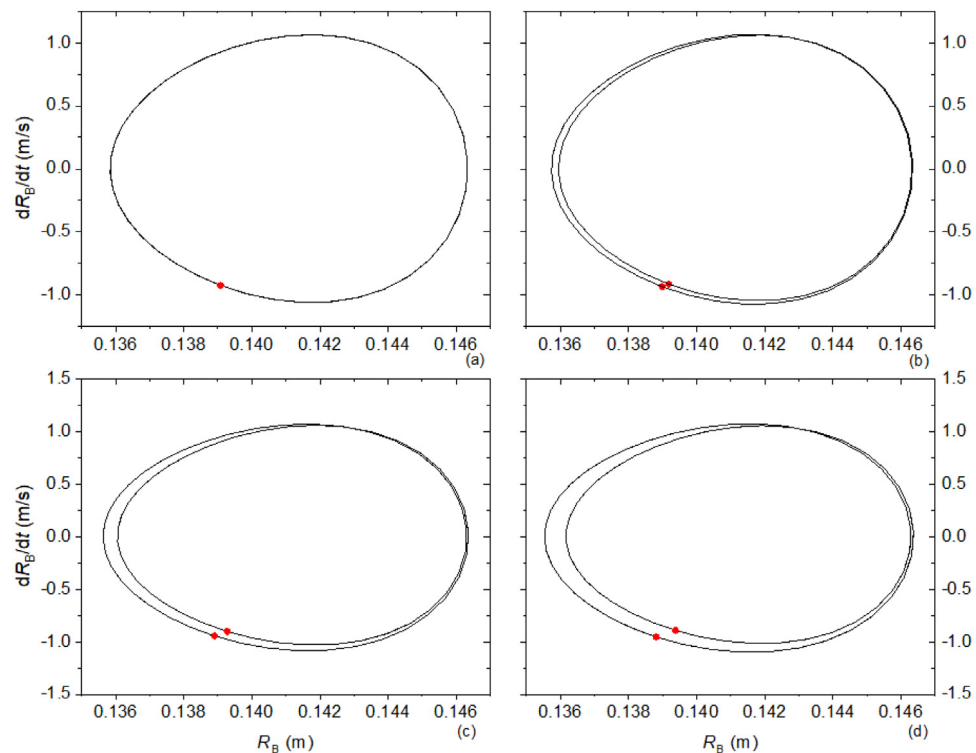
considering that the origami wheel robot path is described by the projection of the G point (path followed by the mass center of the robot). Basically, four cases are treated: a desired reference path, Case I (Fig. 13-a); both wheels are heated in the same way inducing a partial phase transformation, Case II (Fig. 13-b); heating induce incomplete phase transformation on wheel A and complete on wheel B, Case

III (Fig. 13-c); heating induce the opposite case of the previous one, complete phase transformation on wheel A and incomplete on wheel B, Case IV (Fig. 13-d).

It should be pointed out that, when the thermal cycle is applied symmetrically, with the same rate and limits on both wheels, the origami robot is able to follow a similar path (final straight line is parallel to the
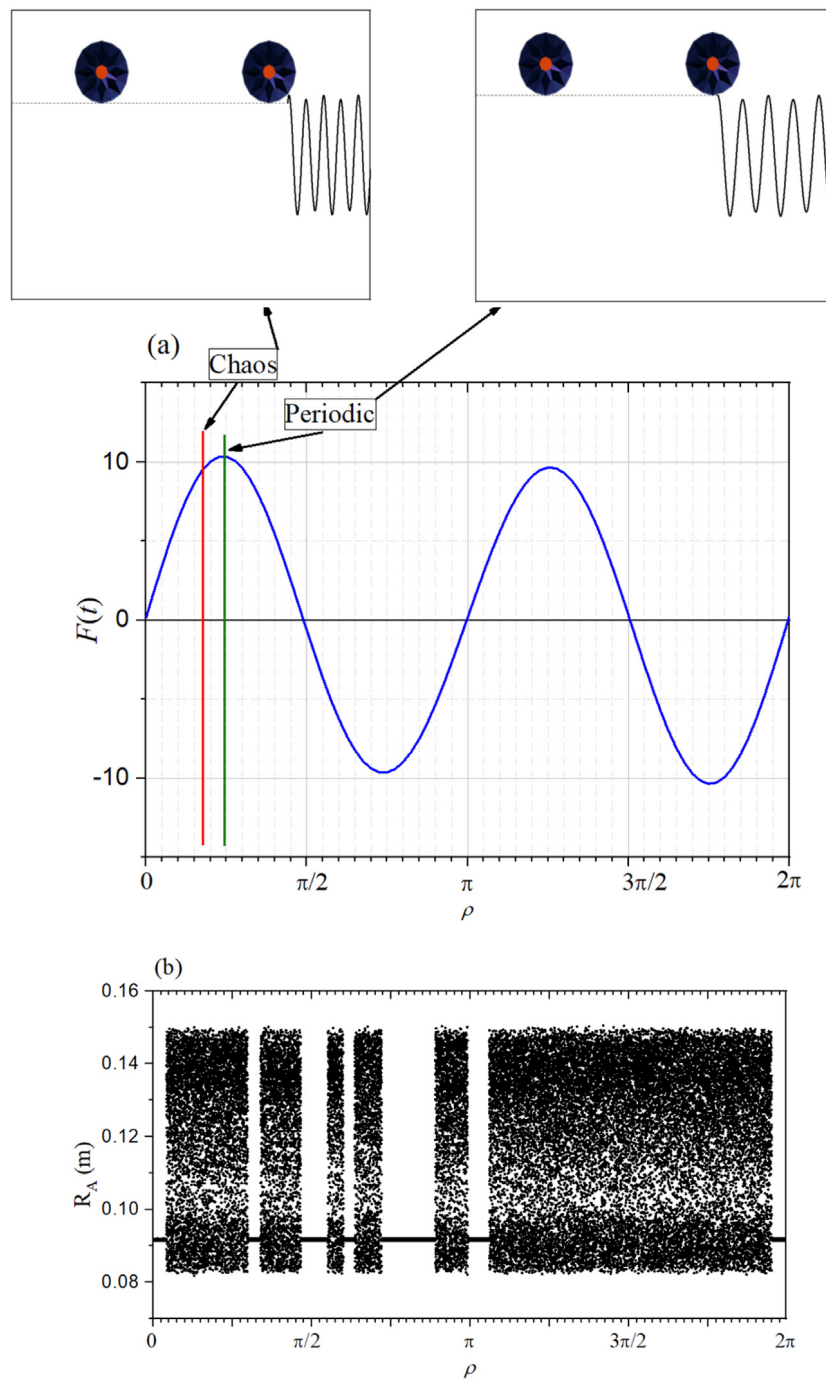
Fig. 23. Dynamic response of the system when subjected to the force $F(t)$. (a) Force on time with a selection of one period (T) with the phase going from 0 to 2π; (b) Spectrum diagram for R_A evaluated on ρ.

excerpt V in Fig. 11-b), despite of the path curvature, returning to the initial orientation (X axis). The partial phase transformation promotes a smaller radius curvature that makes the origami robot to follow a straight path either towards south-east (Case III) or towards north-east (Case IV) with the same inclination related to X axis. After the heating cycle is finished, a plateau of constant temperature is reached where $T > T_A$. Under this condition, it is possible to find a linear relation between the length of the plateau (time that the high temperature is kept constant) and the path curvature described by origami robot.

Nonlinear characteristics of the origami wheel robot can provide complex dynamical behavior and small perturbations can either lead the system to a chaotic behavior or dramatically change its response. In order to explore the influence of these perturbations, a soil interaction is considered and represented by an external mechanical stimulus (external force). Simulations are performed considering $\delta_1 = 10$ N, $\omega_1 = 200$ rad/s and $\omega_2 = 300$ rad/s. The value of the parameter δ_2 is chosen in order to represent different perturbations, changed on each simulation.

Fig. 14 presents an analysis of the influence of the perturbation on the origami wheel robot path in four cases, evaluating deviations from the desired path, evaluated with a constant velocity and $F(t) = 0$, with the thermal cycle presented in Fig. 11. The hatched regions on the domain represent perturbation zones related to different soils that excite the wheel with a force $F(t)$. Four situations are treated considering different levels of perturbation: $\delta_2 = 0$(force is a pure sine, without perturbation), $\delta_2 = 0.5$, $\delta_2 = 1$ and $\delta_2 = 1.5$. For
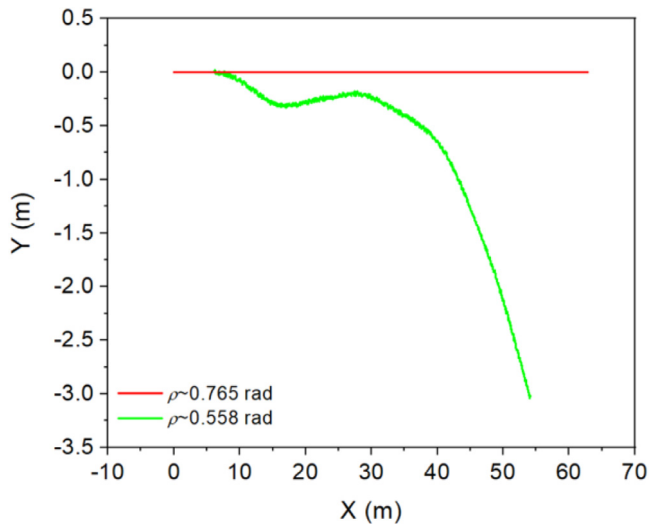
Fig. 24. Path described by the G point for the chaotic and the periodic responses.

all cases, the origami-wheel robot passes through the dashed region at least once, promoting a deviation of the original path. Depending on the angle that the robot entries the dashed region, it can have either one or both wheels over the perturbed soil. Fig. 14 also shows a zoom that illustrates an example situation for the case $\delta_2 = 1$. Note that initially, only the wheel A is subjected to the external force and afterwards, both wheels are over the dashed region, being subjected to the same perturbation. When $\delta_2 = 0N$, after the cooling process of wheel A, the wheel A stabilizes at an opened configuration, while wheel B stabilizes at a closed configuration (see Fig. 6), which promotes a curved path. A similar behavior occurs for the case $\delta_2 = 1.5N$, although the origami robot passes through a second dashed region, changing its initial deviation.

Fig. 15 presents a better idea of the external stimulus considering a binary representation of the wheel with respect to the region. This binary representation evaluates only if the wheel is contained within a dashed region or not. For all four cases from Fig. 14, represented respectively on Fig. 15, the wheel A is represented by a blue line, while wheel B is represented by a red line. If the wheel is outside of the region, it is given a value 1. Otherwise, if the wheel touches the dashed region such that an external force acts on it, it is given a value 0. Note that for all four cases, both wheels reach the dashed region. For the cases $\delta_2 = 0$, shown in Fig. 15-a, and $\delta_2 = 0.5$, shown in Fig. 15-b, wheel A is the first to reach the dashed region and also the first to leave it. Besides, for these two cases, only one dashed region is reached. For the case $\delta_2 = 1$, shown in Fig. 15-c, two dashed regions are reached by the wheels. On the first region, wheel A is the first to enter and also the first to leave. On the second region, however, wheel A is subjected to an external force longer than wheel B, once that wheel A is the first to enter and the last to leave that region. This second region is highlighted. Finally, for the case $\delta_2 = 1.5$, shown in Fig. 15-d, two regions interfere with the car motion. The first one acts similarly to the other three cases, where wheel A is the first to enter and also the first to leave the dashed region. However, on the second region, wheel B is subjected to an external force longer than wheel A, once that it stays longer on that dashed region.

The external stimulus acting on the wheels due to the soil interactions promotes oscillations on the wheels, as can be observed in Fig. 16 that shows time evolution of radius R_A and R_B. The dashed lines indicate regions where the wheel is passing through the perturbation region (hatched regions in Fig. 14). Note that the largest deviation related to the desired path occurred on cases where the wheels stabilize at different radius after the first cooling process, indicating that a

correction on the path can be made by controlling the reverse phase transformation, austenite–martensite.

The dynamical behavior of origami wheel A for each of the cases is presented in Fig. 17 where the phase portraits and Poincaré sections are taken considering the first region marked on Fig. 16 (between 12 and 18 s). Similarly, the dynamical behavior for the wheel B is presented in Fig. 18. Note that both wheels have the same qualitative behavior for each case. For $\delta_2 = 0.5N$, the system has a period-2 response, while the other three cases have a chaotic response. These oscillations can be critical for the origami structure since the creased regions are being continuously bended/released [22].

It is clear that the origami-wheel robot has a strong sensitivity to parameter change. Based on that, its design needs to be properly developed in order to avoid undesirable behaviors. In this regard, previous simulations on Fig. 14 are revisited considering a different inertia, $m_G = 0.2$ kg. Under this new condition, the small perturbation condition ($\delta_2 = 0.5$) presents deviation on path that is less aggressive than the one presented by the previous case since the change altered the robot stabilization capacity, stabilizing the wheels after the heating/cooling process (Fig. 19). Besides, the increase on the inertia reduces the sensitivity of the system to external stimulus. For all cases, both wheels stabilize at the same configuration after the first heating/cooling cycle (Fig. 20-a to d), allowing the robot to keep following a straight path. The higher perturbation cases ($\delta_2 = 1N$ and $\delta_2 = 1.5N$) promote a deviation to the right (clockwise rotation) during the second heating/cooling process, once that wheel B stays in an intermediate configuration before stabilizes at an opened one, resulting in a yaw motion clockwise. By changing the inertia, the dynamic response changes from chaotic to period-1 response for the case $\delta_2 = 0N$ and to a period-2 for the other cases. Phase portraits and Poincaré sections for each one of these cases are represented by Fig. 21 for wheel A and Fig. 22 for wheel B.

From now on, all simulations are carried out considering that $m_G = 0.1$ kg. Chaotic systems present a high sensitivity to initial conditions and, as a result, responses starting at two close initial conditions, develop divergent trajectories. By considering the origami wheel robot, this sensitivity can be represented by small changes at position where the soil interaction starts, leading to drastic changes on system behavior, influencing the path described by the origami robot. Previously, the soil perturbations are evaluated through the robot path that crosses different soils and therefore, changes the external stimulus that causes the dynamic behavior of the system. Now, a different situation is of concern considering that the perturbation is kept constant, a case where the system has a periodic response ($\delta_2 = 0.5N$), and the phase of the external excitation changes. Under this assumption, consider a situation where both wheels are excited by the same external force: $F(t) = 10\sin(200t + \rho) + 0.5\sin(300t + \rho)$, where ρ represents a phase. In order to evaluate the influence of this phase ρ, a spectrum diagram is generated monitoring a cut along one period of the external force (Fig. 23-a), starting from the case $\rho = 0$ and increasing the phase until $\rho = 2\pi$. Note that when $\rho = 0$ the system presents a period-2 response (Fig. 17-b). It should be noted that the increase of the phase causes a change on the system response to a chaotic behavior (Fig. 23-b). In both conditions no thermal cycle is applied, meaning that the origami robot must follow a straight line. Fig. 24 shows robot paths by considering two different phases: $\rho \cong 0.765$rad, associated with a periodic behavior of the wheel; and $\rho \cong 0.558$rad, associated with a chaotic behavior. For the periodic response, the robot follows a linear path, while it presents a large deviation on the path for the chaotic case. The upper diagrams in Fig. 23-a are representations of the instant that the wheel enters the perturbed soil, which impacts on the first interaction between the wheels and the soil. On the upper-left diagram, a representation for the chaotic motion, the wheel enters the soil on an instant such that the interaction is similar to an excitation on the wheel starting near the maximum achievable value for the $F(t)$. On the upper-right diagram, a representation for the periodic motion, the
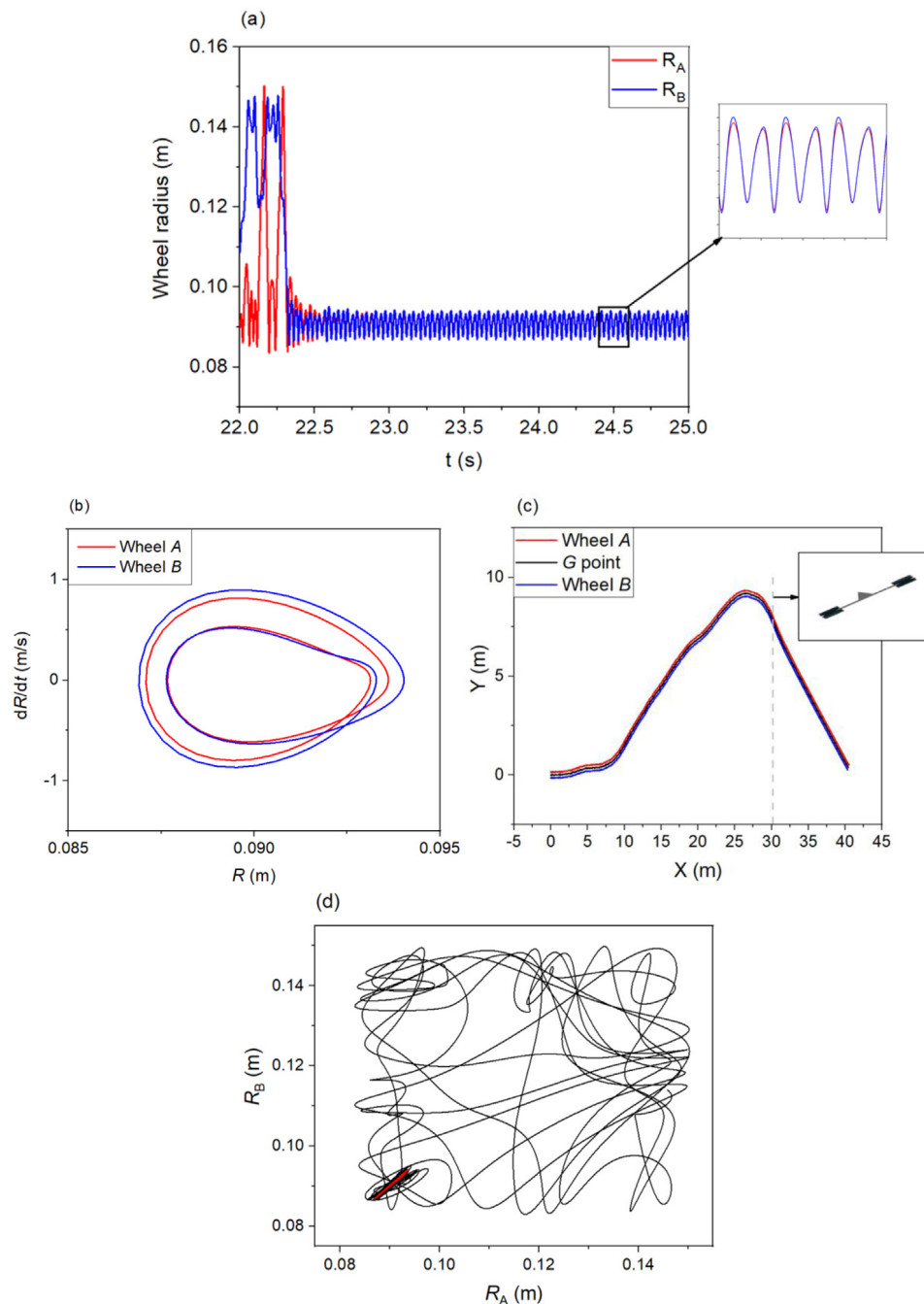
Fig. 25. Synchronization between wheels *A* and *B*. (a) Time evolution of wheels' radius with a zoom at the permanent regime; (b) phase portrait of wheels *A* and *B* at the synchronized configuration; (c) path described by the origami robot; (d) radius manifold showing the synchronization.. (For interpretation of the references to color in this figure legend, the reader is referred to the web version of this article.)

wheel enters the soil on an instant such that the interaction between the rough soil and the wheel is similar to an excitation on the wheel starting at the maximum achievable value for $F(t)$, i.e., the peak. This first interaction is important to define the general behavior of the car while rolling over the rough soil.

Origami wheel robot has its paths defined by the dynamical behavior of the wheels. Therefore, it is essential to understand their global dynamical behavior. An interesting phenomenon related to the origami dynamics is the synchronization of the wheel behaviors. This means that there is a trend that both wheels have the same qualitative response in steady state. According to the previous simulations, it is concluded that a perturbation of $\delta_2 = 0.5$ is associated with a periodic behavior of the wheel while a perturbation of $\delta_2 = 1.5$ is related to

a chaotic behavior (see Fig. 17). Now, a situation where each wheel is subjected to a different perturbation is of concern. Under this condition, it is expected that one wheel presents a periodic response while the other presents a chaotic response. The coupling between the wheels promotes a synchronization of their dynamical behavior, leading to similar responses of both wheels.

Therefore, consider a situation where $F_A(t) = 10\sin(200t) + 0.5\sin(300t)$ and $F_B(t) = 10\sin(200t) + 1.5\sin(300t)$. Thermal effects are not considered which means that a constant temperature is applied to both wheels ($T = 288$ K). Fig. 25 presents results of this simulation showing that the system presents a transient chaos during approximately 22 s and, afterwards, the wheels synchronize, presenting a period-2 response (Fig. 25-a). Through the zoom of the steady state, it is noticeable that
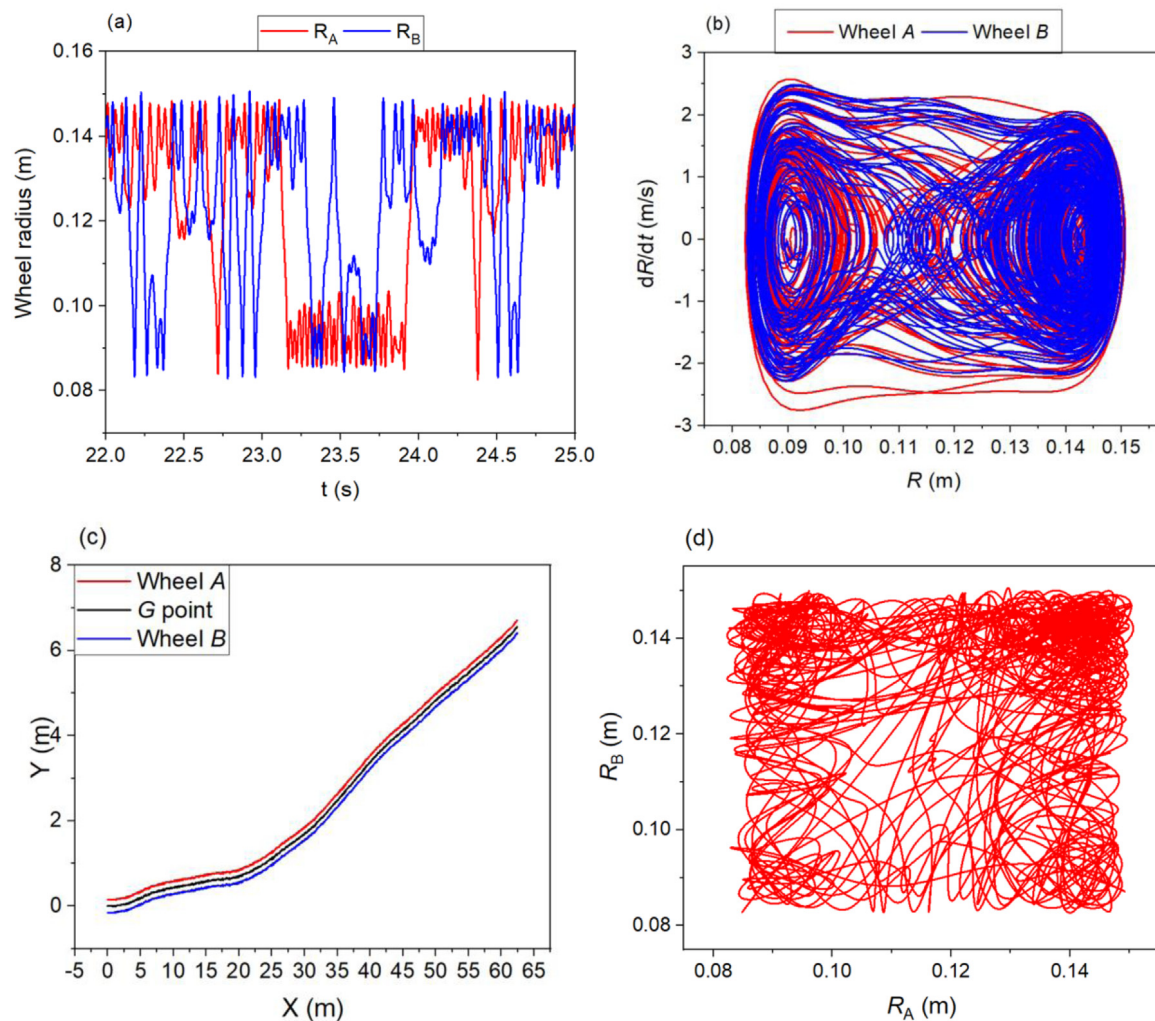
Fig. 26. Chaotic behavior of wheels A and B. (a) Time evolution of wheels' radius with a zoom at the permanent regime; (b) phase portrait of wheels A and B at the synchronized configuration; (c) path described by the origami robot; (d) radius manifold.

the system presents a phase synchronization, which corresponds to a locking of phases of chaotic oscillators [23]. Fig. 25-b presents phase space of each wheel confirming the differences of both orbits. The path followed by the origami robot is shown at Fig. 25-c, where the final configuration is highlighted at the dotted line, and, since both wheels stabilize at the same configuration (both closed), the origami robot follows a straight line after the synchronization. Fig. 25-d shows the radius space illustrating the transient response (in black) and the synchronization manifold $R_A = R_B$ (in red).

By considering a condition where $F_A(t) = 10 \sin(200t) + 1.0 \sin(300t)$ and $F_B(t) = 10 \sin(200t) + 1.5 \sin(300t)$ with constant temperature to both wheels ($T = 288$ K), the system presents a chaotic steady state response (Fig. 26). Fig. 26-a shows the radii evolution; Fig. 26-b presents phase space of each wheel confirming the chaotic-like response. The path followed by the origami robot is shown at Fig. 26-c, illustrating the difference between this path with the previous one. Fig. 26-d shows the radius space illustrating the chaotic behavior that tends to occupy all the space.

6. Conclusions

This paper deals with the dynamical analysis of an origami wheel robot actuated by shape memory alloys. A mathematical model is proposed considering robot rigid body motion and deformable origami wheels that can promote path control. Each origami wheel is described

by a reduced-order model developed on symmetry hypothesis. Under this assumption, the origami wheel is represented by a one-degree of freedom system. Polynomial constitutive model is employed to describe the thermomechanical behavior of shape memory alloy actuators. Combining the rigid body model with origami wheel description, a four degrees of freedom system is achieved to describe the robot motion. A mechanical external stimulus is employed to represent different kinds of wheel–soil interaction. Numerical simulations are carried out for different conditions showing that the system has a rich dynamics. A perturbation analysis is performed considering different external stimuli. Essentially, these perturbations alter the robot path, promoting dramatic deviations due to differences between the wheels' radii. Besides that, complex responses are investigated, including chaos, transient chaos and synchronization. In general, it is possible to conclude that origami wheel robot has several interesting properties to be exploited for different purposes, but its paths are defined by the dynamical behavior of the wheels, which have strong nonlinearities and therefore, needs to be deeply investigated for application purposes. A temperature control applied to the system can be useful to adjust the path and avoid undesirable situations.

CRediT authorship contribution statement

Larissa M. Fonseca: Conceptualization, Formal analysis, Investigation, Methodology, Software, Validation, Writing - original draft,

Writing - review & editing. **Marcelo A. Savi:** Conceptualization, Formal analysis, Funding acquisition, Investigation, Methodology, Project administration, Resources, Software, Supervision, Validation, Writing - original draft, Writing - review & editing.

Declaration of competing interest

The authors declare that they have no known competing financial interests or personal relationships that could have appeared to influence the work reported in this paper.

Acknowledgment

References

[1] A. Sorguç, I. Hagiwara, S. Selçuk, Origamis in architecture: a medium of inquiry for design in architecture, METU J. Fac. Archit. 26 (2) (2009) 235–247.

[2] S.M. Felton, D.-Y. Lee, K.-J. Cho, R.J. Wood, A passive, origami-inspired, continuously variable transmission, Int. Conf. Robot. Autom. (2014) 2913–2918.

[3] Y. Nishiyama, Miura folding: applying origami to space exploration, Int. J. Pure Appl. Math. 79 (2012) 269-179.

[4] M. Salerno, K. Zhang, A. Menciassi, J.S. Dai, A novel 4-DOFs origami enabled, SMA actuated, robotic end-effector for minimally invasive surgery, IEEE International Conference on Robotics and Automation (2014) 2844–2849.

[5] T. Tachi, Geometric considerations for the design of rigid origami structures, in: Proceedings of the International Association for Shell and Spatial Structures Symposium, 2010.

[6] M. Schenk, S.D. Guest, Folded textured sheets, in: Proceedings of IASS Symposium, 2009.

[7] R.C. Albermani, H. Khalilpasha, H. Karampour, Propagation buckling in deep sub-sea pipelines, Eng. Struct. 33 (9) (2011) 2547–2553.

[8] E.T. Filipov, K. Liu, T. Tachi, M. Schenk, G.H. Paulino, Bar and hinge models for scalable analysis of origami, Int. J. Solids Struct. 124 (2017) 26–45.

[9] K. Kuribayashi, K. Tsuchiya, Z. You, D. Tomus, M. Umemoto, T. Ito, M. Sasaki, Self-deployable origami stent grafts as a biomedical application of Ni-rich TiNi shape memory alloy foil, Mater. Sci. Eng. A 419 (2006) 131–137.

[10] S. Miyashita, S. Guitron, M. Ludersdorfer, C.R. Sung, D. Rus, An untethered miniature origami robot that self-folds, walks, swims, and degrades, in: International Conference on Robotics and Automation, 2015.

[11] D.Y. Lee, J.S. Kim, S.R. Kim, J.S. Koh, K.-J. Cho, The deformable wheel robot using magic-ball origami structure, in: Proc. of the ASME 2013 Int. Design Engineering Technical Conf. & Computers and Information in Engineering Conf. (IDETC/CIE), 2013.

[12] S.K. Malu, J. Majumdar, Kinematics, localization and control of differential driven mobile robot, Global J. Res. Eng. 14 (1) (2014).

[13] G.V. Rodrigues, L.M. Fonseca, M.A. Savi, A. Paiva, Nonlinear dynamics of an adaptive origami-stent system, Int. J. Mech. Sci. 133 (2017) 303–318.

[14] L.M. Fonseca, G.V. Rodrigues, M.A. Savi, A. Paiva, Nonlinear dynamics of an origami wheel with shape memory alloy actuators, Chaos Solitons Fractals 24 (2019) 5–261.

[15] H. Fang, Y. Zhang, K.W. Wang, Origami-based earthworm-like locomotion robots, Bioinspiration Biomim. 12 (6) (2017).

[16] F. Falk, Model free-energy, mechanics and thermodynamics of shape memory alloys, Acta Metall. 28 (12) (1980) 1773–1780.

[17] R.A.A. Aguiar, M.A. Savi, P.M.C.L. Pacheco, Experimental and numerical investigations of shape memory alloy helical springs, Smart Mater. Struct. 19 (2) (2010) 025008.

[18] Z. Chen, J. Gu, X. Yang, A novel rigid wheel for agricultural machinery applicable to paddy field with muddy soil, J. Terramech. 87 (2020) 21–27.

[19] Y. Favaedi, A. Pechev, M. Scharringhausen, L. Richter, Prediction of tractive response for flexible wheels with application to planetary rovers, J. Terramech. 48 (2011) 199–213.

[20] K. Nishiyama, H. Nakashima, T. Yoshida, T. Ono, H. Shimizu, J. Miyasaka, K. Ohdoi, 2d FE–DEM analysis of tractive performance of an elastic wheel for planetary rovers, J. Terramech. 64 (2016) 23–35.

[21] G. Sharma, S. Tiwary, A. Kumar, H.N.S. Kumar, K.A.K. Murthy, Systematic design and development of a flexible wheel for low mass lunar rover, J. Terramech. 76 (2018) 39–52.

[22] K.C. Francis, J.E. Blanch, S.P. Magleby, L.L. Howell, Origami-like creases in sheet materials for compliant mechanism design, Int. J. Mech. Sci. 4 (2) (2013) 371–380.

[23] M.G. Rosemblum, A.S. Pikovsky, J. Kurths, Phase synchronization of chaotic oscillators, Phys. Rev. Lett. 76 (1995) 1804–1807.